

## **Integration of grid maps in merged environments**

Tanja Wernle<sup>1</sup>, Torgeir Waaga\*<sup>1</sup>, Maria Mørreaunet\*<sup>1</sup>, Alessandro Treves<sup>1,2</sup>, May-Britt Moser<sup>1</sup>  
and Edvard I. Moser<sup>1</sup>

<sup>1</sup>Kavli Institute for Systems Neuroscience and Centre for Neural Computation, Norwegian University of Science and Technology, Trondheim, Norway;

<sup>2</sup>SISSA – Cognitive Neuroscience, via Bonomea 265, 34136 Trieste, Italy

\* Equal contribution

Corresponding author: Tanja Wernle [tanja.wernle@ntnu.no](mailto:tanja.wernle@ntnu.no); Edvard I. Moser, [edvard.moser@ntnu.no](mailto:edvard.moser@ntnu.no)

Manuscript length: 5719 words, 6 figures, 9 supplemental figures.

## Abstract (150 words)

Natural environments are represented by local maps of grid cells and place cells that are stitched together. How transitions between map fragments are generated is unknown. Here we recorded grid cells while rats were trained in two rectangular compartments A and B (each 1 m x 2 m) separated by a wall. Once distinct grid maps were established in each environment, we removed the partition and allowed the rat to explore the merged environment (2 m x 2 m). The grid patterns were largely retained along the distal walls of the box. Nearer the former partition line, individual grid fields changed location, resulting almost immediately in local spatial periodicity and continuity between the two original maps. Grid cells belonging to the same grid module retained phase relationships during the transformation. Thus, when environments are merged, grid fields reorganize rapidly to establish spatial periodicity in the area where the environments meet.

## Introduction

Self-location is dynamically represented in multiple functionally dedicated cell types<sup>1,2</sup>. One of these is the grid cells of the medial entorhinal cortex (MEC)<sup>3</sup>. The multiple spatial firing fields of a grid cell tile the environment in a periodic hexagonal pattern, independently of the speed and direction of a moving animal. This spatial periodicity of the grid pattern is often thought to provide a metric to the brain's navigation system<sup>2,4,5</sup>. In updating the representation of the animal's current position, grid cells are thought to interact locally with other medial entorhinal cell types, such as head direction cells<sup>6</sup>, speed cells<sup>7</sup> and border cells<sup>8,9</sup>, as well as, more remotely, the place cells of the hippocampus, which in turn feed back to the entorhinal cortex<sup>10,11</sup>. Collectively these multiple cell types form a distributed internal map of space that animals may use to guide navigation<sup>1,2,12</sup>.

Grid cells may encode firing locations by integrating linear and angular self-motion cumulatively through a process referred to as path integration<sup>3,4,13-15</sup>. Without reference to external landmarks, the continuous integration of self-motion inputs may accumulate error, grid fields may drift in space, and the grid pattern may eventually break down<sup>4,16,17</sup>. The fact that grid cells maintain stable firing locations both within and between experimental sessions<sup>3</sup> suggests that the brain has mechanisms for preventing such drift. Stability in firing positions may be provided by visual or other sensory inputs from stationary features of the environment, such as the walls and corners of the recording box or discrete landmarks<sup>18-21</sup>. Associations between firing locations and boundaries and landmarks are likely formed during the first exposure to the environment. When the animal returns for a second visit, the cell fires at the same locations<sup>3</sup>. When the environment is extended or compressed by moving the walls, the grid pattern is often distorted accordingly, suggesting that the locations of the grid fields are influenced by the locations of the walls<sup>18,20</sup>.

The influence of walls and other geometric references on the firing locations of grid cells depends on the size and the shape of the environment. In small open boxes, the grid pattern of an individual cell is most often symmetric and coherent, in the sense that the grid maintains a consistent orientation and phase throughout the environment<sup>21,22</sup>. In larger boxes, or in boxes with nonparallel walls, the

alignment with external geometry –or the ‘anchoring’ of the grid map – may be more complex and more variable<sup>19,21</sup>. In environments consisting of two boxes linked by an external corridor, grid cells with identical firing patterns in the two boxes eventually form a single continuous map with no break in the grid phase at the border between the compartments<sup>23</sup>. In other types of compartmentalized environments, individual grid cells have different grid phases in different parts of the environment, and this difference in anchoring seems not to change with training. For example, in mazes where rats traverse successive alleys to reach a destination, the grid pattern of individual cells has been shown to fragment into mosaics of stable sub-grids that reset at the turning points between the alleys of the maze<sup>13</sup>. A similar fragmentation is often present in large open environments, where distortions in the grid pattern are mostly local and imposed by the nearest walls in the enclosure<sup>21</sup>. The regional variation in external anchoring of the grid is consistent with the local nature of remapping among place cells in the hippocampus after perturbations in compartmentalized environments<sup>24-26</sup>.

Little is known about how fragments of grid cells are integrated. When grid cells form discrete maps for different parts of the environment, how are these map fragments linked together when the division between the parts is removed so that the compartments fuse into one continuous open environment? If the periodicity of grid cells is used to estimate distance and direction<sup>5</sup>, how is the continuity of the map maintained from one fragment to another? Are the firing locations of grid cells with different phase and orientation relationships to the environment adjusted at the transition from one fragment to the other, such that a hexagonal periodic firing pattern is always present locally? These questions have been asked also in studies where boxes were linked through a narrow corridor<sup>23</sup>; however, for two-dimensional firing patterns, such as those of grid cells, corridors are non-ideal when the aim is to determine changes in phase relationships in the transition zone. To investigate such changes in an open space, we trained rats in two adjacent rectangular boxes, A and B, under conditions that resulted in grid patterns with different grid phase, grid spacing or grid orientation in the A and B compartments. We then asked whether the phase offset of these grid patterns was maintained when the entire wall between the two rectangular boxes was removed, or whether spatial periodicity emerged locally at the transition between the two original maps in the center of the environment.

## Results

Neural activity was recorded from MEC in 11 rats and from the MEC-parasubiculum border region in 2 rats (**Supplementary Table 1** and **Supplementary Fig. 1**). The latter animals had no grid cells, only head direction cells.

During the training stage of the experiment, the rats were tested on alternating trials in two adjacent rectangular compartments, A and B (1 m x 2 m), while they foraged for biscuit crumbs. A and B were separated by a central wall (**Fig. 1a**). Distal cues were visible from both compartments. After repeated trials in A and B (8 to 23 trials in each compartment), the central wall was removed and the rats explored the merged space (2 m x 2 m, box AB) for up to 9 consecutive sessions. Finally, the rats were tested again in the rectangular compartments A and B. The tetrodes were then lowered, and a new set of grid cells was recorded with the same procedure.

## Reorganization in grid cells

A total of 128 grid cells from 10 rats were recorded in A, B, and AB. Mean grid spacing across environments ranged from 48 cm to 122 cm (**Supplementary Table 1** and **Supplementary Fig. 2 a,b**). Before removal of the wall, compartments A and B were in most cases represented by non-identical grid patterns (**Fig. 1b** and **Supplementary Fig. 2a,c**). The majority of the grid cells had different grid phases in the two environments (phase offset between A and B normalized to grid spacing:  $25 \pm 1\%$  of grid spacing, mean  $\pm$  s.e.m.,  $n = 128$  cells, 10 rats,  $t(127) = 22.8$ ,  $P = 7.8 \times 10^{-47}$ , Student's  $t$ -test two-sided for this and all subsequent analyses;). Grids in A and B occasionally also differed in grid orientation or grid scale, although neither was significantly different at the group level (grid scale A vs. B:  $t(254) = -1.3$ ,  $P = 0.17$ , Student's  $t$ -test; grid orientation A vs. B:  $F(1,254) = 3.3$ ,  $P = 0.06$ , Watson-Williams test).

Removing the central wall changed the firing locations of the grid cells but the effect depended on the distance from the location of the former partition wall. Along the distal walls of the merged enclosure, parallel to the former partition, the cells largely fired in the same location as in the rectangular configuration, suggesting that in these regions the maps for the A and B boxes maintained their anchoring to the external walls of the environment (**Fig. 1b** and **Supplementary Fig. 2 a,d**). In contrast, near the center of the box, the firing fields were generally at different locations than in the original map. To quantify these differences between periphery and center, we used a sliding window procedure (**Fig. 1b** and **Supplementary Fig. 2a, d**). For each cell, the rate map was divided into  $2 \text{ cm} \times 2 \text{ cm}$  bins. A square window with side length similar to the cell's grid spacing was then defined around each bin (e.g.  $31 \times 31$  bins for a cell with 62 cm grid spacing). For each window, the cell's firing rate was correlated with the firing rate in the corresponding window of the divided environment (A|B). The resulting heat map of local correlation values showed high correlation values along the peripheral walls, far away from the partition, and low correlation values in the center of the box, where the window included bins from both A and B of the divided environment (**Fig. 1b,c** and **Supplementary Fig. 2a,d**).

For further analysis, we defined bands of bins parallel or orthogonal to the orientation of the partition wall. The width of each band was 10% of the distance between the peripheral walls. Within the two central parallel bands, along either side of the partition axis, the local correlation between A | B and AB was low:  $0.49 \pm 0.01$  on the A side and  $0.46 \pm 0.01$  on the B side (**Fig. 1c, d** and **Supplementary Fig. 2d**; mean  $\pm$  s.e.m.,  $n = 128$  cells, 10 rats). The highest A | B - AB correlations were observed along the two peripheral walls that were parallel to the partition wall. The mean correlation in these distal 10<sup>th</sup> percentile bands was  $0.72 \pm 0.01$  on the A side and  $0.66 \pm 0.01$  on the B side. The correlation between A | B and AB was significantly higher in distal bands than central bands ( $t(510) = 15.2$ ,  $P = 1.6 \times 10^{-42}$ , Student's  $t$ -test) and increased gradually with distance from the partition wall (**Fig. 1d**;  $r = 0.43$ ,  $P = 9.2 \times 10^{-59}$ ). There was no corresponding change from center to periphery in the orthogonal direction ( $r = -0.001$ ,  $P = 0.97$ ). The grid pattern in the merged environment AB was generally not a mere extension of one of the original maps (**Supplementary Fig. 3a,b**). Taken together, these analyses suggest that near the peripheral borders the grid retained its anchoring.

We also asked if the drop in correlation in the central bands depended on the similarity of the A and B maps. Similarity was estimated by correlating the autocorrelograms of map A and map B with each other (Online Methods). There was a significant correlation between the correlation of A|B and AB in the central 10<sup>th</sup> percentile bands, on one hand, and the autocorrelogram similarity of A and B on the other (**Fig. 1e**;  $r = 0.40$ ,  $P = 2.57 \times 10^{-6}$ ). Autocorrelogram similarity did not correlate significantly with A|B - AB correlation in the distal 10<sup>th</sup> percentiles ( $r = 0.16$ ,  $P = 0.06$ ). Within the subset of cells with high similarity in spacing, orientation, and grid ellipticity (values > 0.7 for each,  $n = 90$  cells, 10 rats), there was a significant negative correlation between phase offset and A|B - AB correlation in the center ( $r = -0.24$ ,  $P = 0.01$ ), suggesting that the most extensive reorganization occurred when the maps on the two sides were incongruent, or out of phase.

When the central wall was reintroduced after successive trials in the merged environment, the original grid maps A and B were fully re-expressed (**Supplementary Fig. 3c**)

Taken together, these analyses suggest that when the two compartments were merged, the A and B maps maintained independent anchoring to the respective distal walls and that conflicts between the A and B maps were not solved in a winner-take-all manner.

### Translocation of grid fields in the transition zone

We next asked which factors determine reorganization of the grid pattern in the center of the box. Specifically, we investigated the possibility that the grid maps from environments A and B became locally coherent by translocating central fields that were out of phase with each other into a single, spatially periodic pattern (referred to as a 'fusion' of the A and B maps). We began by identifying individual grid fields in both environments A|B and AB based on their size and shape (**Fig. 2a** and Online Methods). For each field in rectangular environments A and B, a vector was then defined between the center of that field in the rectangle and the center of the nearest field in the merged AB map within a radius corresponding to 60 % of the cell's grid spacing in A, B, and AB (**Fig. 2b** and **Supplementary Fig. 4a-g**). As predicted if the A and B maps fused into a single map at the same time as they maintained their anchoring to the distal walls, these displacement vectors appeared longer in the center of the box than along the peripheral walls.

To determine quantitatively if such a difference was present, we calculated the average length and direction of the displacement vectors (**Fig. 2c-e** and **Supplementary Fig. 4g**). Vector lengths were normalized to the cell's average grid spacing in A, B, and AB. All vectors were sorted according to their starting position in A or B into square windows of side length 16 cm covering all possible locations in the environment. The average displacement vector was significantly longer for starting positions in the central bands parallel to the partition wall than in the distal bands of the environment (**Fig. 2e**; each band was 1 x 12 bins; center bands:  $27 \pm 0.4$  % of grid spacing, distal bands:  $15 \pm 0.5$  %, mean  $\pm$  s.e.m.,  $n = 128$  cells, 10 rats,  $t(46) = 16.7$ ,  $P = 3.2 \times 10^{-21}$ , Student's *t*-test). Vector lengths increased from periphery to center ( $r = 0.87$ ,  $P = 1.7 \times 10^{-47}$ ). To determine if vectors pointed preferentially in one direction, we computed the mean resultant vector length (MVL) for vectors within four blocks covering 200 x 50 cm in the direction parallel to the inserted wall (**Fig. 2d** and **Supplementary Fig. 4a-f**). The mean resultant vector was significantly non-uniform on both sites of the former partition wall (central A blocks: MVL = 0.61,  $P = 2.4 \times 10^{-68}$ ,  $Z = 139.7$ ; central B blocks: MVL = 0.21,  $P = 3.3 \times 10^{-7}$ ,  $Z = 14.8$ , Rayleigh test). The orientation of the mean vectors was

almost orthogonal to the orientation of the former partition wall, with vectors pointing towards the wall axis on both the A and B side (offset from wall axis in central A band:  $256.6 \pm 50.5$  degrees, central B band:  $96.8 \pm 71.7$  degrees; wall axis defined as 0 degrees). The displacement of firing fields in the center of the box was also accompanied by a change in peak firing rates of grid fields that could be matched before and after removal of the wall (**Supplementary Fig. 4h**).

To ensure that the translocation of firing fields in the central part of the environment was not an artifact of how we identified firing fields, we complemented the displacement analysis with a sliding cross-correlation approach that circumvented identification of firing fields (**Fig. 2f** and **Supplementary Fig. 4a-f** and Online Methods). In this analysis, we determined, for square windows of  $31 \times 31$  bins (1 bin = 2cm) in the two-rectangle A|B environment, the shift that gave the maximum correlation with the rate map of the merged AB environment. (Like in the field-based analysis, the shifts were longer in the central bands parallel to the partition wall than in the distal bands of A and B (central bands:  $23 \pm 1\%$  of grid spacing, distal bands:  $15 \pm 0.7\%$ , mean  $\pm$  s.e.m.,  $n = 128$  cells, 10 rats,  $t(254) = 7.3$ ,  $P = 2.8 \times 10^{-12}$ , Student's  $t$ -test).

Taken together, the field analysis and the cross-correlation analysis indicate that the original A and B maps were integrated by translocation of fields in the transition zone. Along the distal boundaries of the environment, the grid fields remained stably anchored.

### **Grid fields in the merged environment are equidistant**

Next, we asked whether the shift in the location of the grid fields made the distribution of firing field distances in the central region more periodic, with equal distances between firing fields, as would be expected if the pattern converged towards a hexagonal grid solution. To measure spatial periodicity of the grid activity at different locations in the environment, we determined, for each grid field, the distance to its neighboring fields within 130% of the cell's grid spacing in A, B and AB and quantified the standard deviations of field distances ((**Fig. 3a-c**, and **Supplementary Fig. 5a** and Online Methods). As expected, before wall removal when the two original maps A and B were out of phase, the average standard deviation of field distances was significantly larger in the central A and B bands, than in the distal bands (**Fig. 3b**; each band was  $1 \times 12$  bins; central bands: standard deviation of  $0.20 \pm 0.001$ , distal bands:  $0.15 \pm 0.002$ , mean  $\pm$  s.e.m.,  $t(46) = 16.5$ ,  $P = 5.1 \times 10^{-21}$ , Student's  $t$ -test). After wall removal, the standard deviations decreased significantly in the center (**Fig. 3c**; central bands:  $0.16 \pm 0.002$ , mean  $\pm$  s.e.m., central bands before vs. after wall removal:  $t(46) = 15.6$ ,  $P = 4.8 \times 10^{-20}$ , Student's  $t$ -test).

The translocation of single grid fields into a pattern that is locally continuous throughout the environment. is consistent with analyses calculating offsets between grid fields in actual rate maps in either A|B or AB, on one hand, and grid fields in template rate maps based on extension of the original grid pattern in either A or B (**Supplementary Fig. 5b, c**)).

Taken together these data suggest that the grid patterns of the A and B environments became locally continuous in the center by translocating single fields towards an equidistant field pattern.

### A merged grid pattern was present already on the first trial

We next asked whether a continuous grid pattern emerged in the central transition zone already during the first trial in the merged environment AB. To estimate the development of firing rate distribution after wall removal on a fine timescale, we produced rate maps for successive cumulative time intervals of 60 s in the merged environment (60s, 120s, 180s, etc.) (Fig. 4a and Online Methods). Already within the first few minutes after wall removal, grid field locations changed in the central transition zone (Fig. 4b). To determine the development of firing rate distribution separately for the center and the periphery of the box, we correlated the central or the distal part of the interval rate map (each part 100 cm x 200 cm) with the corresponding part in the original map A|B or the final merged map AB. When the rats explored the merged box for the first time, the firing rate distribution in the center was already after three minutes more similar to the final map AB than to the original map A|B (Fig. 4c and Supplementary Fig. 6; correlation with AB:  $0.56 \pm 0.05$ , correlation with A|B:  $0.27 \pm 0.05$ , mean  $\pm$  s.e.m.,  $n = 19$  cells, 10 rats,  $t(36) = -3.78$ ,  $P = 5.69 \times 10^{-4}$ , Student's  $t$ -test). A similar enhancement was observed at the same time in the distal parts of the box (Fig. 4d, correlation with AB:  $0.59 \pm 0.04$ ; correlation with A|B:  $0.38 \pm 0.05$ , mean  $\pm$  s.e.m., AB vs. A|B:  $t(36) = -3.16$ ,  $P = 0.003$ , Student's  $t$ -test; AB center vs. AB distal:  $t(36) = 0.41$ ,  $P = 0.68$ ), possibly reflecting shearing of the grid pattern along the walls<sup>21</sup>. Subsequent to the first trial, there was little change in the firing locations of the grid cells (Supplementary Fig. 7). Taken together these findings demonstrate that when an animal encountered merged space for the first time, the two original maps A and B were integrated on a fast time scale and subsequent changes were only modest.

### Phase relationships of pairs of grid cells were preserved when grid maps merged

Because a preserved phase relationship between grid cells may be crucial for maintaining position information within modules of the grid-cell network<sup>5</sup>, we asked if the translocation of grid fields in the center of the merged environment was coherent across pairs of grid cells. We first identified a subset of cells that belonged to the same module (Supplementary Fig. 8a-f and Online Methods). For each cell pair, we next estimated phase offset by cross-correlating the cells' rate maps in either A, B, the A part of AB, or the B part of AB – areas that each covered 200 x 100 cm (Fig. 5a). To determine if phase offsets were preserved after wall removal, we then measured, for each cell pair, the difference in displacement (distance and orientation) between A and the A region of AB, and between B and the B region of AB (Figure 5b – e). We finally tested statistically if this difference in displacement was smaller than if one of the two cells was replaced randomly with another cell from the same animal in the AB environment. The analysis showed that phase offsets were preserved. The difference in distance and orientation displacement between recorded pairs of cells was significantly lower than for pairs where cell identities had been shuffled (Fig. 5b- e). The pairwise difference in the distance offset between recorded pairs was small, with median values of 2.6 cm in the A part of the environment (10 - 90<sup>th</sup> percentiles: 0.2 – 7.3 cm) and 2.6 cm in the B part (10 - 90<sup>th</sup> percentiles: 0.3 – 8.4 cm), significantly shorter than between random cell pairs (Figure 5c; random pairs median difference in distance in A: 8.1 cm, 10 - 90<sup>th</sup> percentiles: 1.2 – 20.5 cm ; in B: 9.6 cm , 10 - 90<sup>th</sup> percentiles: 1.5 – 22.9 cm; original pairs vs. random pairs in part A:  $Z = 9.02$ ,  $P = 1.76 \times 10^{-19}$ ; part B:  $Z = 9.50$ ,  $P = 1.97 \times 10^{-21}$ , Wilcoxon rank sum test,  $n = 48$  cells, 176 pairs,). The change in orientation was also significantly smaller in the recorded data than the shuffled data (Fig. 5c). When the analysis was confined to the central parts of A and B the differences in distance and orientation offset were

also preserved (**Fig. 5d, e**) suggesting that the high cross-correlations were not caused merely by fields close to the distal walls, which did not move much).

Finally, we confirmed these observations in a separate analysis where we estimated offset by first calculating mean distance between nearest-neighbour grid fields for each combination of simultaneously recorded cell pairs and then correlating those distances across trials in A and AB, or B and AB. This analysis revealed strong correlations between offsets of grid fields before and after removal of the partition (**Fig. 5f,g**; A vs. AB:  $r = 0.85$ ,  $P = 3.0 \times 10^{-29}$ ; B vs AB:  $r = 0.78$ ,  $P = 2.6 \times 10^{-21}$ ), again indicating that phase relationships between pairs of grid cells were preserved.

Taken together, these analyses suggest that within grid modules, grid cells merged coherently into a single continuous map when the wall was removed. The number of simultaneously recorded cells was too small to determine the extent of coherence in cell pairs from different modules.

### Reorganization in other entorhinal cell types

The local nature of the reorganization of the grid map was consistent with changes in other spatial cell types of the MEC. When the partition wall was removed, border cells maintained their firing pattern along the distal walls whereas firing fields along the central partition disappeared in the absence of the wall (**Fig. 6a** and **Supplementary Fig. 9a**; spatial correlation distal 10<sup>th</sup> percentile bands:  $0.55 \pm 0.05$ , central 10<sup>th</sup> percentile bands:  $0.09 \pm 0.04$ , mean  $\pm$  s.e.m.,  $n = 9$  cells, 3 rats, central vs. distal percentiles:  $t(34) = -6.3$ ,  $P = 2.9 \times 10^{-7}$ , Student's *t*-test)

The change in grid cells and border cells was accompanied by a similar reorganization in non-periodic, spatially modulated cells that did not pass criteria for grid cells, border cells or head direction cells (**Fig. 6b** and **Supplementary Fig. 9b** and Online Methods, grid scores:  $-0.18 \pm 0.03$ , border scores:  $-0.13 \pm 0.04$ , mean vector length :  $0.10 \pm 0.01$ , mean  $\pm$  s.e.m.,  $n = 15$  cells, 11 rats The mean A | B - AB correlation in the distal 10<sup>th</sup> percentile bands was  $0.44 \pm 0.03$ , significantly higher than in the central 10<sup>th</sup> percentiles ( $0.28 \pm 0.03$ ,  $t(58) = -2.9$ ,  $P = 0.004$ , Student's *t*-test). Correlation values increased with distance from the partition wall ( $r = 0.30$ ,  $P = 0.0002$ ).

In contrast to grid cells and border cells, head direction cells maintained their distinct firing properties after the partition was removed (**Fig. 6c,d** and **Supplementary Fig. 9c**). The mean vector length of the directional tuning curve did not change between the last trial in A and B and the first trial in AB (**Fig. 6d**; mean resultant vector length A:  $0.37 \pm 0.01$ , B:  $0.31 \pm 0.01$  and AB:  $0.37 \pm 0.01$ , mean  $\pm$  s.e.m.,  $n = 69$  cells, 8 rats, one-way ANOVA:  $F(2,204) = 4.78$ ,  $P = 0.009$ ;  $P > 0.01$  for all comparisons, Tukey-Kramer *post hoc* test following one-way ANOVA). The directional preferences were also upheld. (**Fig. 6d** correlation of directional distribution of firing rates A vs. B:  $0.69 \pm 0.03$ , A vs. AB:  $0.78 \pm 0.02$ , B vs. AB:  $0.74 \pm 0.03$ , mean  $\pm$  s.e.m., one-way ANOVA:  $F(2,204) = 2.44$ ,  $P = 0.08$ ;  $P > 0.07$  for all comparisons, Tukey-Kramer *post hoc* test following one-way ANOVA). Stable preferred firing direction was observed also in a small subset of conjunctive head direction  $\times$  grid cells with grid scores above 0.25 and mean vector lengths above 0.23 (**Fig. 6e,f**).

Taken together, these analyses suggest that the entire medial entorhinal position map – consisting of grid cells, border cells and other spatial cells – remained anchored to the distal walls when the



central wall was removed, and that, in all spatially modulated cells, the firing pattern reorganized in the center of the box, where the two maps met. The directional tuning of the entorhinal map remained unaffected.

## Discussion

This study shows that when animals are permitted to move freely between previously discontinuous enclosures, the grid maps of those enclosures remain largely anchored to the stable walls at the periphery of the environment. At the same time, they fuse into a locally coherent grid pattern in the central area where the maps meet. During the initial stage of the experiment, when the animals were tested separately in A and B, stable grid maps were formed for each environment. Grids in A and B usually differed in grid phase, grid orientation, or grid spacing. When the partition was removed, the maps maintained their firing pattern along the outer walls, but in the center, along the partition axis, the locations of the firing fields changed, moving towards a more equidistant pattern, with local periodicity reestablished. The reorganization of the grid maps was expressed already during the first trial in the merged environment, suggesting that it takes place on a fast time scale. Grid cells belonging to the same grid module merged coherently. The change in the grid pattern was accompanied by reorganization of firing locations also in other spatially modulated cells.

First of all, these findings verify that grid cells are controlled by local boundaries. The control by external walls was maintained when animals walked freely between parts of the box that had initially been anchored to different sets of external cues, suggesting that geometric box information took precedence over input from the path integration system. This observation is consistent with previous work showing that environments are often represented in grid cells as a mosaic of locally periodic fragments where, for each fragment, the constellation of firing fields is determined by a unique set of local cues<sup>13</sup>. In open enclosures, fragmentation of the grid pattern may be expressed within cells as differences in the orientation of the grid along opposite walls of the enclosure<sup>21</sup>. Similar control by salient boundaries is observed when an environment is enlarged or compressed and grid patterns rescale correspondingly<sup>18,20</sup>. In the rescaled map, grid cells may maintain their firing locations relative to the nearest walls, consistent with a predominant role for local geometry in the control of phase and orientation in grid cells. An equivalent preponderance for local cues has been observed in ensembles of hippocampal place cells when animals are tested in compartmentalized environments. Changes in the shape or color in one compartment may cause place-cell remapping in that compartment but may leave spatial activity patterns unaffected in the rest of the environment<sup>25,26</sup>. The maintained firing along the distal walls of the present experiment, under conditions when the central area undergoes change, is consistent with these observations from place cells and suggests that spatial maps are anchored locally, both in MEC and hippocampus.

The principal aim of the present study was to determine how locally anchored grid cells resolve inconsistencies in the grid pattern that emerge when environments with different grid spacing, orientation and phases are merged into a single open surface. One possibility would be a complete preservation of the grid patterns from the rectangular environments. If this were the case, the periodicity of the pattern would for most cells be broken in the middle of the merged environment since the grids would be differently oriented and out of phase. This lack of continuity might

compromise path integration-based distance estimates when the animal crosses between the two halves of the environment. The results show, however, that as soon as the wall is removed, the discontinuity between the original maps fades out and a coherent pattern of equidistant fields develops throughout the box. The resulting map is locally continuous in all parts of the merged enclosure, even though the grid patterns of the distal bands remain out of phase. Local continuity may be sufficient for supporting path integration, considering that the accuracy of the grid pattern declines rapidly with distance from external reference points<sup>17</sup>. Over longer distances, inputs from stationary sensory cues, such as the walls, may be required to stabilize the grid<sup>3</sup> but this calibration may occur locally, allowing for incoherence between grid fields in distant parts of the environment.

Local fusion may not represent a universal solution to the lack of periodicity that emerges when grid maps of different environments are out of phase. In a recent study, Carpenter and colleagues<sup>23</sup> trained rats in adjacent square environments connected by an external corridor. Rats ran freely between the two environments. During early stages of the training, grid patterns for the two compartments were identical but out of phase. After 2-3 weeks of training, the phase of the grids changed such that a single continuous pattern formed, despite the detour that the animals had to make through the corridor. The results differ from the present ones in the sense that a single and globally coherent grid pattern emerged for the entire connected environment in that study. The reason for the different outcomes is not clear but it could reflect stronger anchoring to the different geometric cues of the two compartments in the present study. The larger size of the present environment may also contribute to preventing global coherence. The two sets of findings show that for integration of local grid maps, multiple solutions are possible, including both formation of a single new map and fusion of the original maps. When fragments of grid maps are merged, as in the present study, those fragments may still be perceived as parts of a whole. The fact that head direction tuning was similar on both sides of the environment is consistent with this possibility.

The fact that grid cells self-organize into locally coherent patterns when the original anchoring to external cues is maintained has implications for the mechanisms by which grids are generated and updated. Existing theoretical frameworks do not provide a detailed account of the integration mechanism. In one set of models, the grid pattern is thought to emerge as an equilibrium state in a continuous attractor network where cells with similar firing locations excite or inhibit each other via recurrent connections<sup>4,15,16,28</sup>. In these models, the firing pattern is updated by a path integration mechanism in which the animal's movement in the environment is translated across the grid-cell network by way of inputs that signal momentary speed and direction. These inputs are thought to operate in conjunction with inputs that convey information about specific external landmarks, such as local boundaries. The attractor models predict an overall coherence in the direction of field displacement in the fusion zone during reorganization of the grid map. Such coherence in changes of phase relationships can be seen across grid cells in simulations when translation of the population pattern is made slower in one direction, e.g. by changing the amplitude of velocity input for that direction<sup>16</sup>. The prediction of coherent changes in the grid pattern is upheld in the present study since pairs of grid cells belonging to the same module maintain a coherent phase relationship when two compartments are merged into one. The fast time course of the reorganization of the grid map is also consistent with the operation of a pre-wired attractor network, in which perturbations of the population pattern appear to be corrected within seconds<sup>29</sup>. However, no existing attractor model speaks specifically to the question of whether and how a stable and coherent grid pattern is formed

when the original maps are incongruent. Anchoring is not explicitly modelled in attractor networks but one could hypothesize that ‘anchoring forces’ might change the gain of the translation of the population pattern, e.g. by coupling it to velocity input. Removing the central wall might influence these anchoring forces, leading to a change in the gain of the translation of the population pattern, which might be read out in single cell responses as translocation of firing fields.

In an alternative model, grid patterns are formed in cells that adapt to spike frequency<sup>30</sup>. In the presence of Hebbian plasticity, competition between spatial inputs to adapting cells leads gradually to the formation of hexagonal firing patterns. Because the process is local in the recording environment, it might account for the emergence of periodic firing in the transition zone. One potential conundrum is that this form of self-organization may require many iterations of synaptic weight changes. Such changes may take place during experience-dependent wiring of synaptic connections during postnatal maturation of the network but it might be too slow to account for de novo grid formation at the timescale of seconds or minutes in specific environments<sup>31</sup>. A further challenge is that, in the present experiment, a pre-existing grid structure may already be present at the distal ends of the enclosure, raising the question of how pre-existing patterns in the network are balanced against conflicting sensory inputs. The open nature of these questions is shared with the insufficiency of the attractor models. Finding out how grid cells resolve local incongruences in the periodicity of the grid pattern would benefit from further theoretical development.

#### **Accession Codes**

Custom code that supports the main finding are available on <https://doi.org/10.11582/2017.00023>.

#### **Data Availability Statement**

The data that support the main finding are available on <https://doi.org/10.11582/2017.00023>.

#### **Acknowledgments**

We thank S. Rosay and Y. Bitterman for discussion and M.P. Witter for advice on histology. We thank A.M. Amundsgård, K. Haugen, E.Kråkvik, B.B. Løfaldli, H. Waade, and V. Frolov for technical assistance. The work was supported by the European Commission’s FP7 FET Proactive Programme on Neuro-Bio-Inspired Systems (GRIDMAP - Grant Agreement 600725), an Advanced Investigator Grant from the European Research Council (GRIDCODE – grant no. 338865), the Centre of Excellence scheme and the National Infrastructure Scheme of the Research Council of Norway (Centre for Neural Computation, grant number 223262; NORBRAIN1, grant number 197467), the Louis Jeantet Prize, the Körber Prize, and the Kavli Foundation.

## Author contributions

Ta.W., M.-B.M. and E.I.M. designed the experiment, Ta.W. and To.W. collected data, Ta.W. analyzed data, To.W. and M.M. contributed to analysis development, M.-B.M. and E.I.M. supervised the project, A.T. advised on analyses, and Ta.W. and E.I.M. wrote the paper with the input from all authors.

## Competing Financial Interests Statement

The authors declare no competing financial interests.

## References

- 1 Moser, E. I. *et al.* Grid cells and cortical representation. *Nat Rev Neurosci* **15**, 466-481, doi:10.1038/nrn3766 (2014).
- 2 Rowland, D. C., Roudi, Y., Moser, M. B. & Moser, E. I. Ten Years of Grid Cells. *Annu Rev Neurosci* **39**, 19-40, doi:10.1146/annurev-neuro-070815-013824 (2016).
- 3 Hafting, T., Fyhn, M., Molden, S., Moser, M. B. & Moser, E. I. Microstructure of a spatial map in the entorhinal cortex. *Nature* **436**, 801-806, doi:10.1038/nature03721 (2005).
- 4 McNaughton, B. L., Battaglia, F. P., Jensen, O., Moser, E. I. & Moser, M. B. Path integration and the neural basis of the 'cognitive map'. *Nat Rev Neurosci* **7**, 663-678, doi:10.1038/nrn1932 (2006).
- 5 Stemmler, M., Mathis, A. & Herz, A. V. Connecting multiple spatial scales to decode the population activity of grid cells. *Sci Adv* **1**, e1500816, doi:10.1126/science.1500816 (2015).
- 6 Sargolini, F. *et al.* Conjunctive representation of position, direction, and velocity in entorhinal cortex. *Science* **312**, 758-762, doi:10.1126/science.1125572 (2006).
- 7 Kropff, E., Carmichael, J. E., Moser, M. B. & Moser, E. I. Speed cells in the medial entorhinal cortex. *Nature* **523**, 419-424, doi:10.1038/nature14622 (2015).
- 8 Solstad, T., Boccara, C. N., Kropff, E., Moser, M. B. & Moser, E. I. Representation of geometric borders in the entorhinal cortex. *Science* **322**, 1865-1868, doi:10.1126/science.1166466 (2008).
- 9 Savelli, F., Yoganarasimha, D. & Knierim, J. J. Influence of boundary removal on the spatial representations of the medial entorhinal cortex. *Hippocampus* **18**, 1270-1282, doi:10.1002/hipo.20511 (2008).
- 10 Bonnevie, T. *et al.* Grid cells require excitatory drive from the hippocampus. *Nat Neurosci* **16**, 309-317, doi:10.1038/nn.3311 (2013).
- 11 Zhang, S. J. *et al.* Optogenetic dissection of entorhinal-hippocampal functional connectivity. *Science* **340**, 1232627, doi:10.1126/science.1232627 (2013).
- 12 Tolman, E. C. Cognitive maps in rats and men. *Psychol Rev* **55**, 189-208 (1948).
- 13 Derdikman, D. *et al.* Fragmentation of grid cell maps in a multicompartiment environment. *Nat Neurosci* **12**, 1325-1332, doi:10.1038/nn.2396 (2009).
- 14 Kraus, B. J. *et al.* During Running in Place, Grid Cells Integrate Elapsed Time and Distance Run. *Neuron* **88**, 578-589, doi:10.1016/j.neuron.2015.09.031 (2015).
- 15 Fuhs, M. C. & Touretzky, D. S. A spin glass model of path integration in rat medial entorhinal cortex. *J Neurosci* **26**, 4266-4276, doi:10.1523/JNEUROSCI.4353-05.2006 (2006).
- 16 Burak, Y. & Fiete, I. R. Accurate path integration in continuous attractor network models of grid cells. *PLoS Comput Biol* **5**, e1000291, doi:10.1371/journal.pcbi.1000291 (2009).
- 17 Hardcastle, K., Ganguli, S. & Giocomo, L. M. Environmental boundaries as an error correction mechanism for grid cells. *Neuron* **86**, 827-839, doi:10.1016/j.neuron.2015.03.039 (2015).

- 18 Barry, C., Hayman, R., Burgess, N. & Jeffery, K. J. Experience-dependent rescaling of  
entorhinal grids. *Nat Neurosci* **10**, 682-684, doi:10.1038/nn1905 (2007).
- 19 Krupic, J., Bauza, M., Burton, S., Barry, C. & O'Keefe, J. Grid cell symmetry is shaped by  
environmental geometry. *Nature* **518**, 232-235, doi:10.1038/nature14153 (2015).
- 20 Stensola, H. *et al.* The entorhinal grid map is discretized. *Nature* **492**, 72-78,  
doi:10.1038/nature11649 (2012).
- 21 Stensola, T., Stensola, H., Moser, M. B. & Moser, E. I. Shearing-induced asymmetry in  
entorhinal grid cells. *Nature* **518**, 207-212, doi:10.1038/nature14151 (2015).
- 22 Fyhn, M., Hafting, T., Treves, A., Moser, M. B. & Moser, E. I. Hippocampal remapping and grid  
realignment in entorhinal cortex. *Nature* **446**, 190-194, doi:10.1038/nature05601 (2007).
- 23 Carpenter, F., Manson, D., Jeffery, K., Burgess, N. & Barry, C. Grid cells form a global  
representation of connected environments. *Curr Biol* **25**, 1176-1182,  
doi:10.1016/j.cub.2015.02.037 (2015).
- 24 Skaggs, W. E. & McNaughton, B. L. Spatial firing properties of hippocampal CA1 populations  
in an environment containing two visually identical regions. *J Neurosci* **18**, 8455-8466 (1998).
- 25 Paz-Villagran, V., Save, E. & Poucet, B. Independent coding of connected environments by  
place cells. *Eur J Neurosci* **20**, 1379-1390, doi:10.1111/j.1460-9568.2004.03570.x (2004).
- 26 Spiers, H. J., Hayman, R. M., Jovalekic, A., Marozzi, E. & Jeffery, K. J. Place field repetition and  
purely local remapping in a multicompartiment environment. *Cereb Cortex* **25**, 10-25,  
doi:10.1093/cercor/bht198 (2015).
- 27 Langston, R. F. *et al.* Development of the spatial representation system in the rat. *Science*  
**328**, 1576-1580, doi:10.1126/science.1188210 (2010).
- 28 Couey, J. J. *et al.* Recurrent inhibitory circuitry as a mechanism for grid formation. *Nat  
Neurosci* **16**, 318-324, doi:10.1038/nn.3310 (2013).
- 29 Yoon, K. *et al.* Specific evidence of low-dimensional continuous attractor dynamics in grid  
cells. *Nat Neurosci* **16**, 1077-1084, doi:10.1038/nn.3450 (2013).
- 30 Kropff, E. & Treves, A. The emergence of grid cells: Intelligent design or just adaptation?  
*Hippocampus* **18**, 1256-1269, doi:10.1002/hipo.20520 (2008).
- 31 Si, B. & Treves, A. A model for the differentiation between grid and conjunctive units in  
medial entorhinal cortex. *Hippocampus* **23**, 1410-1424, doi:10.1002/hipo.22194 (2013).

## Figure legends

**Figure 1** Grid maps remain anchored to distal walls but merge along the partition when the partition between two adjacent environments is removed. **(a)** Illustration of experimental procedure. The rat was trained in two rectangular compartments A and B (1 m x 2 m) separated by a central partition. On the test, the partition was removed and the rats explored the merged open square environment AB (2 m x 2 m) for up to 9 consecutive sessions. Scale bar, 50cm. **(b)** Left: Representative firing rate maps in the divided A|B and merged environment AB for two grid cells from two different rats (top and bottom row). Color is coded from dark blue (0) to dark red (peak firing rate). Peak firing rates are indicated at the top and bottom right. Rat identity and cell number are indicated at the top (T = tetrode, C = cell). Small white stippled boxes illustrate example of pair of subspaces that were correlated for a particular position (white dot in left diagram) in the sliding correlation maps in the right part of the figure. Scale bar, 50 cm. Center: Sliding correlation heat map A|B x AB for the cell to the left. Color coding from dark blue to dark red (color bar). Right: Color-coded average sliding correlation heat map for all cells recorded from one rat. Number of cells is indicated at the bottom right. **(c)** Average sliding correlation heat map A|B x AB for all cells and rats, color-coded as in **b**. Black stippled lines illustrate 1 percentile bands, parallel or orthogonal to the insertion wall. Number of cells is indicated at the bottom right. Distal correlations were not significantly different from within-trial correlation values before wall removal (correlation first vs second half of trials in A, distal 10<sup>th</sup> percentile:  $0.73 \pm 0.01$ , trials in B, distal 10<sup>th</sup> percentile:  $0.70 \pm 0.01$ ; within-trial A|B correlations vs. correlations between A|B and AB:  $t(510) = 0.15$ ,  $P = 0.09$ , two sided Student's *t*-test; the two distal segments were combined). **(d)** Average correlation along the distal-to-central axis for 1 percentile bands parallel or orthogonal to the insertion wall as illustrated in **c**. Statistical analyses are performed with 10<sup>th</sup> percentile bands as units. **(e)** Average correlation in center 10<sup>th</sup> percentile bands vs. similarity of A and B maps before wall removal.

**Figure 2** Translocation of individual grid fields in the central zone after wall removal. **(a)** Grid field detection. Representative firing rate maps of two grid cells from two different rats (top and bottom row) in the divided A|B and merged AB environment. Black and red dots indicate detected grid peak locations detected in A|B and AB, respectively. Scale bar, 50 cm. **(b)** Left: Vector maps for the two grid cells in **a**. Black vectors indicate field translocation from the original field position in A or B to the nearest field in AB, within 60% of the cell's grid spacing in A, B, and AB. Right: Average vector map for all vectors in one rat. Rat identity is indicated at the top. Number of cells is indicated at the bottom right. Scale bar, 50 cm. **(c)** Distribution of translation vectors (in black) across blocks of 50 x 50 cm of the recording box for the two average vector maps in (b). Mean resultant vectors (MVL) are added on top of the single vectors as thick red lines. Grey background shading indicates MVL  $P < 0.001$  with Rayleigh test for uniformity. **(d)** as in **c** but for all vectors from all rats ( $n = 128$  cells, 10 rats). The orientation was similar in distal and central bands (orientation central A vs. distal A band:  $F(1,752) = 0.01$ ,  $P = 0.91$ ; orientation central B vs. distal B band:  $F(1,741) = 1.49$ ,  $P = 0.22$ ; Watson Williams test). **(e)** Average normalized vector length map for all vectors from all rats, coded from dark blue to dark red (color bar). Vector lengths were normalized to each cell's average grid spacing in A, B, and AB. Based on their starting position in A or B, vectors were sorted into square windows of side length 16 cm. Vectors within each window were then averaged ( $n = 128$  cells, 10 rats). **(f)** Average sliding cross-correlation map for all cells and all rats, showing relative shift between maps that gave maximum cross-correlation, with normalized shift color-coded from dark blue to dark red (color bar,

1 bin = 2 cm;  $n = 128$ , 10 rats). Shifts were normalized to each cell's average grid spacing in environments A, B, and AB. The outer edges of the rate map (edge  $\pm 15$  bins in x and y direction) were not considered in this analysis (here the cross-correlation windows would cover progressively smaller spatial segments of 29 bins or less and the maximum possible shift would be correspondingly smaller). The shift lengths increased with distance from the distal wall (distance from the central partition line vs. correlation between A|B and AB:  $r = 0.28$ ,  $P = 8.8 \times 10^{-18}$ ; distance from orthogonal wall vs. correlation between A|B and AB:  $r = 0.01$ ,  $P = 0.62$ ).

**Figure 3** Continuity in the transition zone between the two original maps A and B emerged through increased equidistance of grid fields. **(a)** Illustration of grid field distances in the separated A|B environment and the merged AB environment. Top: Representative firing rate maps in A|B and AB. Black and red dots indicate detected grid peaks in A|B and AB respectively. Bottom: Schematic illustrating an example grid field in A|B and AB and the distance to all neighboring fields within 130% of the cell's average grid spacing in A, B, and AB. **(b)** Top: Average standard deviation of grid field distances for all cells and rats before wall removal, color-coded from dark blue (minimum standard deviation in A|B and AB) to dark red (maximum standard deviation in A|B and AB) ( $n = 128$  cells, 1576 fields, 10 rats). Grid field distances were normalized to each cell's average grid spacing in A, B, and AB. Based on their grid field position in A|B, standard deviations were sorted into square windows of side length 16 cm and then averaged. Bottom: Number of fields per 16 cm x 16 cm window color-scaled from white (minimum number of fields) to black (maximum number of fields) ( $n = 128$  cells, 1576 fields, 10 rats). **(c)** as in **b** but after wall removal. ( $n = 128$  cells, 1447 fields, 10 rats). Note that after wall removal the standard deviation of field distances dropped in the center part indicating more equidistant grid spacing. The increase in standard deviations along the distal B side in AB might be due to shearing of the grid pattern in square environments<sup>21</sup> (distal B band in A|B:  $0.15 \pm 0.001$ , distal B band in AB:  $0.18 \pm 0.004$ , mean  $\pm$  s.e.m., distal B band before vs. after wall removal:  $t(22) = -6.28$ ,  $P = 2.5 \times 10^{-6}$ , two-sided Student's *t*-test). The number of fields did not change significantly after wall removal (central bands A|B:  $10 \pm 0.75$  fields, central AB bands:  $8.7 \pm 0.85$  fields, mean  $\pm$  s.e.m., central bands before vs. after wall removal:  $t(46) = 1.17$ ,  $P = 0.24$ , two-sided Student's *t*-test).

**Figure 4** Grid maps in A and B merged rapidly into one map during the first trial in the merged environment AB. **(a)** Development of firing rate distribution during the first trial in AB for two representative grid cells from two different rats (top and bottom row). Left: Firing rate map for the complete trial in the divided A|B environment. Red stippled line indicates center part of the environment covering half of the A and half of the B environment (200 cm x 100 cm). Only visited positions are shown. Right: Firing rate maps for cumulative time intervals during the first trial in AB with the final complete rate map to the right. Time interval lengths are indicated at the top. Only positions that were visited in both the interval map and the complete A|B map were considered. **(b)** Left: Correlation, for the two cells in the top and bottom row of **a**, between the center part of each interval map in AB and the center of the previous A|B map (light red line) or the center of the final AB map (dark red line). Cumulative time intervals start with the first 60s. Black stippled line indicates break on x-axis. Right: same as to the left but for distal parts in the environment. Light and dark grey lines indicate correlation with distal parts of the previous A|B and the final AB map, respectively. Note, in the center where the map reorganized the correlation with the final AB map was larger than

with A|B. In contrast, along the distal walls, where the two maps remained anchored, the correlations were high with both A|B and AB. **(c)** Average correlation for the center part of the merged AB environment on the first trial after wall removal for all cells and rats. Color coding as in **b** (mean  $\pm$  s.e.m.,  $n = 19$  cells, 10 rats, \* indicates the first time point where the correlation with AB was significantly higher than with A|B ( $P = 5.69 \times 10^{-4}$ , two-sided Student's  $t$ -test) **(d)** As in **c** but for distal parts of the environment ( $P = 2.65 \times 10^{-4}$ , two-sided Student's  $t$ -test).

**Figure 5** Pairs of grid cells maintain their phase relationship after wall removal, suggesting that populations of grid cells merge coherently. **(a)** Left: Before wall removal: Representative rate maps for an example cell pair in the divided A|B environment. Center column shows the central part of the cross-correlograms for map A and map B of the same cell pair (top and bottom, respectively). Color is coded from dark blue (-1) to dark red (1). Black line indicates phase offset between two maps and points towards the peak with the shortest displacement from origin. Crossing between black stippled lines illustrates origin of the cross-correlogram. Scale bar, 50 cm. Right: After wall removal: same cell pair as to the left. Scale bar, 50 cm. **(b)** Left: Average difference of distance offset between same (S) and randomly (R) chosen cell pairs for the rat in **a**. Red line indicates median difference in offset of the center peak, box edges indicate 25<sup>th</sup> and 75<sup>th</sup> percentiles, whiskers extend to the most extreme point that lies within 1.5 times the interquartile range, and data points larger than 1.5 times the interquartile range are considered outliers (black dots) ( $n = 11$  cells/ 55 pairs,  $***P < 0.001$ , two-sided Wilcoxon rank sum test). Right: Average angular difference of orientation offset between original and randomly chosen cell pairs for the rat in **a** ( $***P < 0.001$ , Watson  $U^2$  test). **(c)** Same as in **b** but for all 4 rats, 6 trials and 176 cell pairs. The number of simultaneously recorded grid cells ranged from 6 to 11 cells (median orientation difference: in A: 6.9 degrees, 10 - 90<sup>th</sup> percentiles: 0.5 - 19.3 degrees; in B: 7.5 degrees, 10 - 90<sup>th</sup> percentiles: 0.8 - 105.1 degrees; random pairs in A: 93.8 degrees, 10 - 90<sup>th</sup> percentiles: 21.4 - 162.6 degrees; in B: 90.0 degrees, 10 - 90<sup>th</sup> percentiles: 17.0 - 161.2 degrees; original pairs vs. random pairs in A:  $U^2 = 5.19$ ; in B:  $U^2 = 4.11$ , both  $P$  values  $< 0.001$ , Watson  $U^2$  test,  $n = 176$  pairs). **(d)** Phase relationships were maintained when the analysis was confined to the central part of the box (200 cm  $\times$  70 cm on each side of the division). Offsets plotted as in **b**. **(e)** Same as in **d** but for all 4 rats and 6 trials (difference center distance offset: original pairs vs. random pairs in A:  $Z = 7.4$ ,  $P = 1.29 \times 10^{-13}$ ; in B:  $Z = 9.1$ ,  $P = 8.3 \times 10^{-20}$ , two-sided Wilcoxon rank sum test,  $n = 176$  pairs; difference center orientation offset: in A:  $U^2 = 4.64$ ; in B:  $U^2 = 4.62$ , both  $P$  values  $< 0.001$ , Watson  $U^2$  test,  $n = 176$  pairs). **(f)** Scatterplots showing mean offset between grid fields of simultaneously recorded pairs of grid cells in A ( $x$  axis) versus offsets for the same cell pairs in AB ( $y$  axis). Each dot represents the mean offset between a pair of grid cells. Offsets are color coded for rat identity (blue – rat 20607, 11 cells / 55 pairs; green – rat 20077, 7 cells / 21 pairs; orange – rat 20285, 7 cells / 21 pairs). **(g)** as in **f** but for trials in B vs. AB.

**Figure 6** Reorganization of firing distribution in multiple entorhinal functional cell types. **(a)** Border cells. Left: Representative firing rate map for a border cell in the divided A|B environment and the merged AB environment. Note that cells with firing fields along one side of the central wall in B shifted their firing location to the corresponding parallel distal wall in AB when the central wall was removed. Consistent with this observation, the firing rates of border cells with fields along the partition dropped in the center 10<sup>th</sup> percentile bands of the environment after wall removal (change of firing rate center 10<sup>th</sup> percentiles:  $-1.8 \pm 0.54$  Hz, mean  $\pm$  s.e.m.,  $t(16) = 2.7$ ,  $P = 0.01$ , Student's  $t$ -test) but not along the distal walls (distal 10<sup>th</sup> percentiles:  $-0.4 \pm 0.45$  Hz,  $t(16) = 0.57$ ,  $P = 0.57$ ,



Student's *t*-test). Scale bar, 50 cm. Right: Color-coded average sliding correlation heat map A|B × merged box AB for all border cells from all rats color-coded from dark blue to dark red (color bar) ( $n = 9$  border cells, 3 rats). **(b)** Non-periodic, spatially modulated cells that were neither grid cells nor border cells or head direction cells. Left: Representative firing rate map in the divided A|B environment and the merged AB environment. Scale bar, 50 cm. Right: Average sliding correlation heat map A|B × AB for all non-periodic, spatially modulated cells ( $n = 15$  cells, 5 rats), color coded as in **a**. The change in this class of spatial cells did not correlate with their grid scores (A|B - AB correlation for central 10<sup>th</sup> percentiles vs. grid scores:  $r = -0.002$ ,  $P = 0.99$ ). **(c)** Head direction cells. Representative polar plots showing angular firing rate distribution of 4 simultaneously recorded head direction cells. Mean vector length, a measure for directional tuning, is indicated above each plot. Peak firing rate is indicated at the bottom right **(d)** Left: Average directional tuning for all head direction cells in A, B, and AB. Red line indicates mean ( $n = 69$  cells, 8 rats). Right: same as left but for average directional correlation. **(e)** Conjunctive grid x head direction cells (grid score  $> 0.25$  and mean vector length  $> 0.23$ ). Left: as in **b** but for a conjunctive grid cell. Scale bar, 50 cm. Right: as in **c** for the conjunctive grid cell to the left **(f)** as in **d** but for all conjunctive grid x head direction cells (mean  $\pm$  s.e.m.,  $n = 10$  cells, 4 rats; mean vector length: A:  $0.32 \pm 0.02$ , B:  $0.25 \pm 0.02$ , AB:  $0.30 \pm 0.03$ , one-way ANOVA:  $F(2,29) = 1.42$ ,  $P = 0.25$ ;  $P > 0.1$  for all comparisons, Tukey-Kramer *post hoc* test following one-way ANOVA; correlation of directional distributions in A vs. B:  $0.69 \pm 0.05$ , A vs. AB:  $0.74 \pm 0.02$ , B vs. AB:  $0.69 \pm 0.05$ , one-way ANOVA:  $F(2,29) = 0.43$ ,  $P = 0.65$ ;  $P > 0.1$  for all comparisons, Tukey-Kramer *post hoc* test following one-way ANOVA).

## Online Methods

### Subjects

Data were obtained from 13 male Long Evans rats at the age of 3-5 months (400–600 g). All rats were kept on a 12 hr light/12 hr dark schedule in a humidity and temperature-controlled environment. Rats were housed in single animal cages. Testing occurred in the dark phase. The rats were kept at ~90% of their free-feeding body weight and food-deprived 12–18 hr before each training or recording session. The experiments were performed in accordance with the Norwegian Animal Welfare Act and the European Convention for the Protection of Vertebrate Animals used for Experimental and Other Scientific Purposes.

### Surgery and electrode implantation

The rats were anesthetized with 5% isoflurane (air flow: 0.6 l/min) in an induction chamber. Upon induction of anesthesia, they received subcutaneous injections of buprenorphine (Temgesic), Meloxicam (Metacam), and Baytril. The rats were then fixed in a Kopf stereotaxic frame for implantation. Local anesthetic Bupivacaine (Marcaine) was injected subcutaneously before making the incision. During surgery, isoflurane was gradually reduced from 3% to 1% according to physiological condition. The depth of anesthesia was monitored by testing tail and pinch reflexes as well as breathing.

Anesthetized rats were implanted with two microdrives, each carrying a single bundle of 4 tetrodes. The tetrodes were implanted bilaterally in MEC at an angle of 20 degrees relative to the bregma/lambda horizontal reference plane, with the tips pointing in the anterior direction to sample

tangentially from dorsal to ventral entorhinal cell layers. The tetrodes were inserted 4.6 mm lateral to the midline and 0.2 mm anterior to the transverse sinus edge, with an initial depth of 1800  $\mu\text{m}$ . The implant was secured to the skull with jeweler's screws and dental cement. Two screws were connected to drive grounds.

Tetrodes were constructed from four twisted 17  $\mu\text{m}$  polyimide-coated platinum-iridium (90%–10%) wires (California Fine Wire, CA). The electrode tips were plated with platinum to reduce electrode impedances to between 120 and 300 k $\Omega$  at 1 kHz.

### **Behavioral procedure**

The rats were first trained to collect randomly scattered chocolate or vanilla biscuit crumbs on alternating trials in two rectangular boxes A and B (100 cm x 200 cm x 60 cm) for several days (**Fig. 1a**; A|B trials). The boxes shared a continuous black floor mat. The long wall between A and B was referred to as the central wall or the partition wall. The long walls on the opposite sides were referred to as the distal or peripheral walls. All walls were 60 cm high. Testing was performed at low light levels to encourage exploration. The rats had access to the same distal visual cues in both compartments. Recordings in each rectangle lasted 20 min. Before each trial, the rat rested on a flowerpot on a pedestal covered with towels. Between trials, the rat rested in its home cage, which was brought temporarily to the recording room, and the floor mat was cleaned.

Once a stable set of grid cells could be identified across several trials in A and B, the rat was tested on the same day first in A, then in B, and then, for the first time, in a merged version of the two boxes (AB), with the central wall removed before trial start. Removal of the central wall yielded an open square of 200 cm x 200 cm. The trial in the AB environment lasted up to 45 min. The same set of grid cells was recorded in AB for up to 9 consecutive trials on successive days (1 trial each day). Finally, the rat was tested once again in rectangles A and B. Then the tetrodes were lowered in steps of 50  $\mu\text{m}$  while the rat was trained again on alternating trials in A and B until a new set of stable grid cells was recorded. The test procedure was then repeated. The general trial sequence was A|B \_ AB1 \_ AB2 ... A|B \_ AB1\_AB2 ... A|B. The total number of A|B and interleaved AB exposures varied across animals. The maximum number of trials in AB was 24.

### **Recording procedure**

Data collection started within 1 week after surgery. During recording, the animal was connected to an Axona data acquisition system (Axona Ltd., Herts, U.K.) via an AC-coupled unity-gain operational amplifier close to the head, using a light-weight counterbalanced multiwire cable from both implants to an amplifier. Unit activity was amplified 3000 -14,000 times and band-pass filtered between 0.8 and 6.7 kHz. Triggered spikes were stored to disk at 48 kHz with a 32-bit time stamp. An overhead camera recorded the position of two light-emitting diodes (LEDs) on the head stage, each at a sampling rate of 50 Hz. The diodes were separated by 3 cm and aligned with the body axis of the rat. To sample activity along a wide range of dorso-ventral MEC positions, the tetrodes were lowered in steps of 50  $\mu\text{m}$  over the course of the entire experiment, with 2900  $\mu\text{m}$  as the most ventral position.

### **Spike sorting and cell classification**

Spike sorting was performed offline using graphical cluster-cutting software (tint; Neil Burgess and Axona Ltd.). Spikes were clustered manually in two-dimensional projections of the multidimensional parameter space (consisting of waveform amplitudes), using autocorrelation and cross-correlation functions as additional separation tools and separation criteria. Cluster separation was determined by calculating distances between spikes of different cells in Mahalanobis space<sup>32</sup> (median isolation distance: 20.5; 25<sup>th</sup> – 75<sup>th</sup> percentiles: 13.5 – 37.2). Noise in the vicinity of clusters was expressed as the L ratio (median L ratio: 0.18; 25<sup>th</sup> – 75<sup>th</sup> percentiles: 0.09 – 0.38). Clusters on successive recording trials were identified as the same unit if the spike clusters were stable.

### **Rate map construction**

Position estimates were convolved with a Gaussian window covering 35 positions samples and x,y - coordinates were sorted into 2 cm x 2 cm bins. Spike timestamps were matched with position timestamps. Only spikes collected at instantaneous running speed above 5cm/s were included. Firing rate distributions were determined by counting the number of spikes and time spent in each 2 cm x 2 cm bins. Firing rate distributions were smoothed with a two-dimensional Gaussian Kernel with standard deviation of 3.5 bins (7 cm) in both directions x and y.

### **Definition of grid cells**

The spatial periodicity of each rate map – the cell's grid score – was determined by calculating a spatial autocorrelogram<sup>6</sup>. For each cell, a grid score was determined by taking a central circular sample of the autocorrelogram, with the central peak excluded (central peak was defined as 100 or more contiguous pixels of 1.5 x 1.5 cm<sup>2</sup> above a fixed threshold  $r > 0.1$ ), and comparing rotated versions of this sample<sup>6,27</sup>. The Pearson correlation of the circular sample with its rotation in  $\alpha$  degrees was obtained separately for angles of 60 and 120 on one hand and 30, 90 and 150 on the other. The cell's grid score was defined as the minimum difference between any of the elements in the first group (60 and 120 degrees) and any of the elements in the second.

A cell was defined as a grid cell if its grid score exceeded a chance level determined by repeated shuffling of the experimental data (100 permutations per cell). For each permutation, the entire sequence of spikes fired by the cell was time-shifted along the animal's path by a random interval between on one side 20 s and on the other side 20 s less than the length of the session, with the end of the session wrapped to the beginning. Time shifts varied randomly between permutations and between cells. If the grid score from the recorded data was larger than the 95<sup>th</sup> percentile of grid scores in the distribution of shuffled data from all cells, the cell was defined as a grid cell. For a cell to be included in the analysis, its grid score needed to pass the 95<sup>th</sup> threshold of the shuffled distribution in at least one trial in A, B or AB. The 95<sup>th</sup> percentile grid score turned out to be 0.25.

### **Local peak detection in spatial autocorrelograms and firing rate maps**

Peaks were detected in autocorrelograms and firing rate maps based on their size and shape without setting an arbitrarily chosen threshold for local peak detection. To achieve this, autocorrelograms or rate maps were first transformed into a greyscale image of connected regions or objects by applying the morphological image processing operations erosion and reconstruction (Matlab image processing toolbox). Erosion removed small objects in the original image A and resulted in an eroded marker

image  $J$ <sup>33</sup>. The remaining objects in the eroded image  $J$  served to mark objects in in the original image  $A$  and to reconstruct them based on morphological greyscale reconstruction.

Finally, the center bin of each object in the reconstructed image was determined and used to identify the  $x,y$  - location of peaks in the spatial autocorrelograms or firing rate maps. If the center bin in the rate map had a higher mean firing rate than 1 Hz, it was counted as grid field. The firing rate of the center bin indicated the firing rate of the grid field.

#### **Grid axis, spacing, orientation, and $x,y$ - phase offset**

For each grid map, the average grid spacing and grid orientation were determined in the following manner. In the cell's spatial autocorrelogram, local peaks were detected as described above ('Local Peak Detection'). The six peaks closest to the origin of the autocorrelogram determined 'the inner hexagon'. The peak with the shortest positive angular distance to the horizontal axis was defined as grid axis 1. The peaks with the shortest positive or negative angular distance to axis 1 were defined as grid axis 2 and grid axis 3, respectively. The distances from the origin to the three grid axis peaks were defined as the grid spacing of axes 1 - 3. The angular distances of the three grid axes to the horizontal were defined as the grid orientation of grid axis 1 - 3. The average grid spacing was expressed as the arithmetic mean of grid spacing of axes 1 - 3 and the average grid orientation was expressed as the arithmetic angular mean of grid axes 1 - 3.

The  $x,y$ -phase offset between two grid cells was determined by cross-correlating their firing rate maps. If the two rate maps were identical, the center peak in the cross-correlogram would be at the origin. If the two maps were shifted relative to each other in the  $x,y$ -plane, the center peak would be displaced from the origin. To determine the center peak displacement, local maxima defined as bins with a higher value than the 8 neighboring bins were identified in the cross-correlogram. The distance to the maximum closest to the origin was taken as the length of the phase offset between the two grid maps.

#### **Sliding correlation between firing rate maps**

The similarity between the rate maps in the divided box  $A|B$  and the merged box  $AB$  was determined by Pearson correlation. First, a single rate map was produced for the divided environment ( $A|B$ ) by adding the trajectory in  $A$  to the end of the trajectory in  $B$ . Local correlations between  $A|B$  and  $AB$  were then calculated using a sliding window approach. Starting in one corner of map  $A|B$ , we defined a window with side length equal to the cell's grid spacing, e.g.  $31 \times 31$  bins for a cell with 62 cm grid spacing (1 bin = 2 cm  $\times$  2 cm). The firing rates across all bins covered by the window were correlated with those of the corresponding area in the merged environment. Along the outer walls of the recording box, where the window extended beyond the limits of the rate map, only bins on the inside were considered. The window was then moved in steps of 1 bin in the  $x$  and  $y$  directions until all positions of the environment were covered. Using this procedure, a local spatial correlation value could be calculated for every bin in the environment resulting in a heat map of local correlation values (100  $\times$  100 bins). Finally, maps of correlation values from different cells of different animals were averaged.

To compare the change in correlation in the center and the periphery of the box, the average correlation heat map was divided into 10<sup>th</sup>- percentile bands of 10 x 100 bins in the direction parallel or orthogonal to the partition wall (1 bin = 2cm). To determine if correlation values decreased gradually along the distal-to-central axis, the heat map was divided into 1 percentile bands instead (1 x 100 bins) and the average of each band was correlated with the distance to the distal parallel or orthogonal wall.

### Similarity of grid maps

To determine if the amount of reorganization in the center of the merged map AB was depended on the similarity between the original maps A and B, the average correlation in the center 10<sup>th</sup> percentile bands was correlated with the similarity between map A and B. Similarity between map A and B was determined by correlating their autocorrelograms with each other. Each autocorrelogram reflected the cell's grid spacing, grid orientation, and grid ellipticity. If maps A and B had similar grid patterns, their autocorrelograms were positively correlated. For a subset of cells with high similarity values ( $r > 0.7$ ), we cross-correlated the rate maps and determined the distance phase offset. To account for edge effects in autocorrelograms due to lower sampling, autocorrelograms were weighted according to

$$C(x', y') = C(x, y) * \frac{((X - |x|) * (Y - |y|))}{(X * Y)}$$

where  $C(x', y')$  was the weighted correlation value at bin  $x, y$ ,  $C(x, y)$  the original correlation value at bin  $x, y$ , and  $X$  and  $Y$  the dimensions of the original rate maps in bins (1 bin = 2 cm x 2 cm).

### Calculation of extended template grid pattern

To determine if the grid pattern in the merged box AB was a mere extension of one of the two original maps A or B, we simulated extended square grid patterns based on the rectangular grid pattern in A or B. To incorporate grid ellipticity into the extension pattern, we simulated perfectly periodic grid patterns by fitting the average spacing and orientation of axis 1 and 2, as extracted from the autocorrelograms in each rectangle. Then, grid peaks were simulated at the distorted hexagonal lattice nodes. A probability density function was computed in which Gaussian modes were distributed at the  $x, y$ -locations of the lattice nodes. Each mode was described by a two-dimensional Gaussian function

$$f(x', y') = A \exp\left(-\left(\frac{(x - x_0)^2}{2\sigma_x^2}\right) - \left(\frac{(y - y_0)^2}{2\sigma_y^2}\right)\right)$$

where  $A$  is the amplitude,  $x_0$  and  $y_0$  were the coordinates of the lattice nodes and  $\sigma_x^2$  and  $\sigma_y^2$  the Gaussian variance in two dimensions.

We set

$$A = 1$$
$$\sigma_X^2 = \sigma_Y^2 = \left(\frac{\delta}{5}\right)^2$$

where  $\delta$  is the average grid spacing of the three grid axes 1- 3.

The x,y-phase of the simulated grid pattern was determined by cross-correlating it with the original rate map. The local maximum, defined as the bin with a higher value than the 8 neighboring bins, indicated length and direction of the phase offset.

### Calculation of vector maps

To estimate the translocation of individual firing fields, we computed a vector map of field movement for each cell in the following way. Single peaks or firing field locations in the rate maps for A, B, and AB were detected as described above ('Local Peak Detection'). For each grid field, we computed a vector pointing from the field's position in A or B to the nearest field in AB, within a radius corresponding to 60% of the cell's average grid spacing in A, B, and AB. For each vector the length was computed in bins (1 bin = 2cm). If no neighboring field in AB could be identified, the field was not considered. Note that individual vectors originating from fields in A or B could point towards the same field in AB, indicating the merging of grid fields. To compare field movement across different grid cells and grid scales, vector lengths were normalized to each cell's average grid spacing in A, B, and AB. To estimate local average field movement from A or B to AB, vectors from all cells were sorted, according to their starting position in A or B, into square windows of side length 16 cm. For each window the average normalized vector length was computed. The resulting 12 x 12 bin matrix (192 x 192 cm) was smoothed in the x and y directions with a 2D Gaussian Kernel of 5 bins. The remaining  $\pm 4$  cm in the x and y direction along the outer edge of the box were not considered due to uneven coverage across animals. To quantify the change in vector lengths along the distal-to-central axis parallel or orthogonal to the insertion wall, bands of 1 x 12 bins were defined (1 bin = 16 cm) and the average vector length of each band was correlated with the band's distance from the distal parallel or orthogonal wall. To determine if fields were translocated in a preferred direction when the central wall was removed, vector maps were divided into bands of 100 x 25 bins or square blocks of 25 x 25 bins (1 bin = 2cm). For each band or block, the mean resultant vector was computed and a Rayleigh test was used to determine if the underlying distribution was uniform.

### Calculation of local field phase offset

Single grid fields were detected in the rate maps for A|B and AB and in two template patterns based on rate maps in A or B (see below). Each map covered 2 m x 2 m. To determine the phase shift of each field, we computed vectors pointing from each field's position in A|B or AB to the nearest field

in template pattern A or B, within a radius corresponding to 50% of the cell's average grid spacing in A, B, and AB. For each vector the length was computed and normalized to the cell's average grid spacing in A, B, and AB. To quantify the change in phase shift along the distal-to-central axis, orthogonal to the insertion wall (distal wall A to distal wall B), we sorted vectors according to their starting position in A|B or AB, defined 10<sup>th</sup> percentile bands of 10 x 100 bins and calculated the average phase shift for each band.

If the position of single fields was stable before wall removal, the distance between fields in the A part of A|B and template A should be small (and similarly a small distance would be expected for the B part of A|B and template B). Phase shifts would be expected to increase abruptly on the other side of the wall, approximating a step-like function. If single fields were translocated after wall removal to establish local continuity in the center of the box, phase shifts would be expected to increase between AB and template A in the A part, and between AB and template B in the B part, approximating a linear function.

We determined the extent to which the phase shift along the distal-to-central axis approximated a step-like or linear function in the following way: A linear regression was fit to the data from 10% bands spanning the entire environment (from distal north wall in A to distal south wall in B). Based on the linear regression values at the south and north ends, a step-function was constructed, with identical y values for the first 5 and the last 5 bands, respectively. To determine differences between data and either the linear regression value or step-function value residual mean square roots were computed and expressed as percentage of grid spacing. Residual mean square roots were then compared before and after wall removal. To estimate if the change in residual mean square roots in A|B vs. AB was significant, we applied a Student's t-test to the squared residuals before vs. after wall removal.

### **Sliding cross-correlation of rate maps**

To quantify local reorganization of the grid pattern independently of grid field detection, the split A|B rate map was cross-correlated with the rate map of the merged environment AB. Starting in one corner of rate map A|B, square windows of 31 x 31 bins (1 bin = 2 cm x 2 cm) were defined and cross-correlated with equally sized windows across the entire rate map AB, searching for the cross-correlation shift that gave the maximum correlation. Since the grid pattern is periodically repeating, the search for maxima was limited within a window corresponding to half of the box size ( $\pm 15$  bins) in each of the x and y directions which is below one-half of the typical grid spacing in the merged environment ( $38 \pm 0.83$  bins, mean  $\pm$  s.e.m.,  $n = 128$  cells). The analysis was performed for all possible squares of 31 x 31 bins within the A|B environment, allowing for cross-overs between A and B. The outer edges of the rate map (edge  $\pm 15$  bins in x and y direction) were not considered, since the maximum possible shift could only reach  $\pm 14$  bins or less. To compare across different grid scales, shift lengths were normalized to each cell's average grid spacing in A, B, and AB and summed across all windows of the environment for all cells resulting in a 70 x 70 bin heat map of normalized shift lengths. To compare the change in correlation in central and distal parts of the box parallel to the inserted wall, the heat map was divided into bands of 70 x 10 bins (1 bin = 2 cm). To determine if

correlation values decreased gradually along the distal-to-central axis, the heat map was divided into bands of 70 x 1 bins.

### **Analysis of local periodicity**

Standard grid symmetry scores<sup>6,27</sup> require minimum surface areas corresponding to a full circle with radius similar to the grid spacing and would not be suitable to quantify local spatial periodicity at different locations in the environment. Instead, to determine if removal of the partition wall increased the spatial periodicity of firing fields in the center of the environment, resulting in more equidistant grid field distances, we detected firing field locations in the split rate map A|B and the rate map of the merged environment AB were detected as described above ('Local Peak Detection'). For each grid field, the distance to all neighboring fields within 130% of the cell's average grid spacing in A, B, and AB was determined. Fields with less than two neighbors were not considered. Grid field distances were normalized to each cell's average grid spacing in A, B, and AB and for each field the standard deviation of these distances was computed. Fields with less than three neighbors were not considered. To estimate local periodicity, standard deviations from all grid fields and cells were sorted according to their grid field position in A|B or AB into square windows of side length 16 cm. For each window the average standard deviation was computed. The resulting 12 x 12 bin matrix (192 x 192 cm) was smoothed in x and y direction with a 2D Gaussian Kernel of 5 bins. The remaining  $\pm 4$  cm in x and y direction along the outer edge of the box were not considered due to uneven coverage across animals. To quantify the local change in standard deviations, bands of 1 x 12 bins (1 bin = 16 cm) were defined and the average standard deviation between bands in the center and the periphery of the box were compared.

### **Analysis of development of grid pattern formation**

To estimate the development of firing rate distribution in the first trial AB after wall removal, firing rate maps were computed for cumulative time intervals. Interval lengths started with 60s and increased cumulatively in steps of 60s, with the last interval covering the entire trial time. Only positions that were visited in both A|B and AB were considered. Rate maps were constructed as described above ('Rate map construction'). These maps were compared to the complete rate map of the divided A|B environment or the final merged map AB. To estimate local grid pattern development, we considered only the center part (covering half of part A and part B, 200 x 100 cm) or either the distal A and the distal B part (together 200 x 100 cm). To compare development of firing rate distribution across animals, we considered only the first 20' after partition removal, which was the maximum time available in all animals.

### **Analysis of module identity**

The relatively low number of simultaneously recorded grid cells precluded the use of multidimensional clustering algorithms to identify grid modules<sup>20</sup>. Thus, to sort simultaneously recorded grid cells into grid modules sharing the same spacing and orientation, autocorrelograms were correlated in a pairwise manner. Each autocorrelogram reflected the cell's grid spacing, grid orientation, and grid ellipticity. Autocorrelograms were weighted as described above ('Similarity of grid maps'). An ensemble of simultaneously recorded grid cells was considered to belong to the same



module if their average correlation exceeded the 90<sup>th</sup> percentile correlation value of all pairwise correlations of all recorded grid cells across all animals. The 90<sup>th</sup> percentile correlation turned out to be 0.75.

### **Analysis of coherence between pairs of grid cells**

To determine whether ensembles of simultaneously recorded grid cells with the same orientation and spacing responded coherently to merged space, we estimated their pairwise phase relationship before and after wall removal. The analysis was restricted to cells from 6 trials in 4 animals with a minimum number of simultaneously recorded cells (6 to 11 cells). The phase offsets between all pairs of simultaneously recorded grid cells in this sample was determined by cross-correlating their rate maps in A, B, the A part of AB, or the B part of AB – areas that each covered 200 x 100 cm. Local maxima, defined as bins with a higher value than the 8 neighboring bins, were determined, and the local maximum nearest to the origin of the cross-correlogram indicated phase offset. The distance and direction (relative to a horizontal reference plane) of the center peak displacement (the peak nearest the origin) was calculated for each environment, as well as the differences between offsets in A and part A of AB, and between B and part B of AB was determined. The differences were then compared to the difference between randomly chosen cell pairs where one cell was retained in the original cell pair and the other was selected randomly among the simultaneously recorded cells in AB. If the phase offset of the cell pair was lost after removal of the wall, there should be no difference between observed values and those obtained for a random combination of cells.

### **Analysis of grid field offset between pairs of grid cells**

If grid fields from simultaneously recorded cells (sharing the same orientation and spacing) were translocated coherently after wall removal, the pairwise distance between grid fields should remain constant between trials in A, B, and AB. Grid fields were detected in A, B, and AB. To determine the distance between grid fields for simultaneously recorded cell pairs  $i, j$  in A, B and AB, we computed for each trial vectors pointing from each field's position in cell  $i$  to the nearest field in cell  $j$  within a radius corresponding to 50% of the cell's average grid spacing in A, B, and AB. For each vector the length was computed in bins (1 bin = 2cm). The average vector length between cell pair  $i, j$  indicated the mean offset between those cells. Average pairwise offsets were determined for A, B and AB and correlated between A and AB, and between B and AB. The number of simultaneously recorded cells ranged from 6 to 11.

### **Definition of non-periodic, spatially modulated cells**

Non-periodic, spatially modulated cells were defined as cells that did not pass criteria for grid cells nor border cells, or head direction cells (grid scores < 0.25; border scores < 0.39; mean vector length < 0.23) in any of the A, B, and AB trials. Further, for inclusion in this category, the estimated information content needed to exceed the 95<sup>th</sup> percentile of the distribution of information content in the shuffled version of the same data in at least one trial in A, B or AB. Shuffling was performed by

shifting spike times at random intervals along the path in the same way as for grid cells. The 95<sup>th</sup> percentile information content value was 0.66.

Information content was determined for each rate map by computing the spatial information content as

$$\sum_{i=1}^N p_i \frac{\lambda_i}{\lambda} \log_2 \left( \frac{\lambda_i}{\lambda} \right)$$

where  $\lambda_i$  the mean firing rate in the  $i$ -th bin,  $\lambda$  the overall mean firing rate and  $p_i$  the probability of the animal being in the  $i$ -th bin (occupancy in the  $i$ -th bin/total recording time). Spatial activity patterns were stable within session in all parts of the environment (spatial correlation between first and second half of trial of  $0.49 \pm 0.03$  mean  $\pm$  s.e.m.,  $n = 15$  cells).

### **Analysis of head direction cells and conjunctive head x grid cells**

The animal's head direction was determined for each tracked sample by plotting the relative positions of the two LEDs onto the horizontal plane. The directional tuning function for each cell was obtained by plotting the firing rate as a function of the animal's heading direction, divided into bins of 6 degrees and smoothed with a boxcar moving average of 3 bins on each side (= 18 degrees). Directional tuning was estimated by computing the length of the mean resultant vector for the circular distribution of firing rates. For a cell to be included as a head direction cell, its mean resultant vector length needed to pass the 95<sup>th</sup> percentile threshold of the mean resultant vector length in the shuffled version of the same data in at least one trial in A, B or AB. Shuffling was performed by shifting spike times at random intervals along the path in the same way as for grid cells. The 95<sup>th</sup> percentile mean resultant vector length turned out to be 0.23. Conjunctive head x grid cells were defined as cells that at the same time passed the criteria for grid cells and head direction cells (grid scores  $> 0.25$ ; mean resultant vector length  $> 0.23$ ) in at least one trial in A, B or AB.

To determine if head direction cells or conjunctive grid cells changed their directional tuning between A, B, and AB, the mean resultant vector lengths of the three trials were tested statistically with multiple comparison Tukey-Kramer *post hoc* test following one-way ANOVA. To test if the preferred firing direction changed between trials A, B, and AB, directional firing rate distributions in A, B, and AB were correlated with each other.

### **Analysis of border cells**

Border cells were identified by computing a border score for each cell<sup>8</sup>. In rate maps for environments A, B and AB, firing fields were defined as a minimum of 9 neighboring bins (1 bin = 2 cm) with firing rates higher than 20% of the cell's peak firing rate. The cell's border score was expressed as the difference between the maximal length of a wall touching on any single firing field of the cell and the average distance of the field from the nearest wall, divided by the sum of those values. Border scores ranged from - 1 for cells with infinitely small central fields to +1 for cells with infinitely narrow fields that lined up perfectly along the entire wall. Border cells were identified as

cells in which the border score exceeded the 95<sup>th</sup> percentile of the distribution of border scores in shuffled version of the same data in at least one trial in A, B, or AB. The 95<sup>th</sup> percentile border score turned out to be 0.39. Shuffling was performed by shifting spike times at random intervals along the path in the same way as for grid cells.

To determine if border cells shifted their firing fields, the divided A|B map was correlated with the merged AB map applying the sliding-correlation approach as described above ('Sliding correlation between firing rate maps'). To quantify the change in correlation along the distal-to-central axis (parallel to the inserted wall), we divided the heat map of local correlation values into 10<sup>th</sup>-percentile bands of 10 x 100 bins (1 bin = 2cm). For each band the average correlation was determined. To compute the change in firing rate along the distal-to-central axis, rate maps for A, B, and AB were divided into similar bands and the mean firing rate was computed for each band. Border cells with firing fields in the orthogonal direction to the inserted wall were not considered.

### **Histology and Reconstruction of Recording Positions**

The tetrodes were not moved after the final recording session. The rat received an overdose of Pentobarbital and was perfused intracardially with 9% saline and 4% formaldehyde. The brain was extracted and stored in 4% formaldehyde. Frozen, 30mm sagittal sections were cut, mounted on glass, and stained with cresyl violet (Nissl). The final position of the tip of each tetrode was identified on photomicrographs obtained with Axio Scan.Z1 microscope and Axio Vision software (Carl Zeiss, Germany) (**Supplementary Fig. 1**).

### **Statistical tests**

All statistical tests were two-sided. We used Student's t-test, one-way ANOVA with Tukey Kramer post-hoc test for large samples with limited deviations from normality and Wilcoxon signed rank test and Watson U<sup>2</sup> test for distributions that had low n's or deviated more. P-values for Pearson's correlations were computed using a Student's t distribution for a transformation of the correlation (Matlab 'corr' function). No statistical methods were used to pre-determine sample sizes but our sample sizes are similar to those reported in previous publications<sup>21,22</sup>. A **Life Sciences Reporting Summary** is available for an overview of ethics and statistics.

### **Data availability**

Data supporting the main findings is available on <https://doi.org/10.11582/2017.00023>.

### **Code availability.**

Custom code supporting the main findings is available <https://doi.org/10.11582/2017.00023>.

### **Methods-only references**

- 32 Schmitzer-Torbert, N., Jackson, J., Henze, D., Harris, K. & Redish, A. D. Quantitative measures of cluster quality for use in extracellular recordings. *Neuroscience* **131**, 1-11, doi:10.1016/j.neuroscience.2004.09.066 (2005).
- 33 Vincent, L. Morphological grayscale reconstruction in image analysis: applications and efficient algorithms. *IEEE Trans Image Process* **2**, 176-201, doi:10.1109/83.217222 (1993).

**Figure 1**

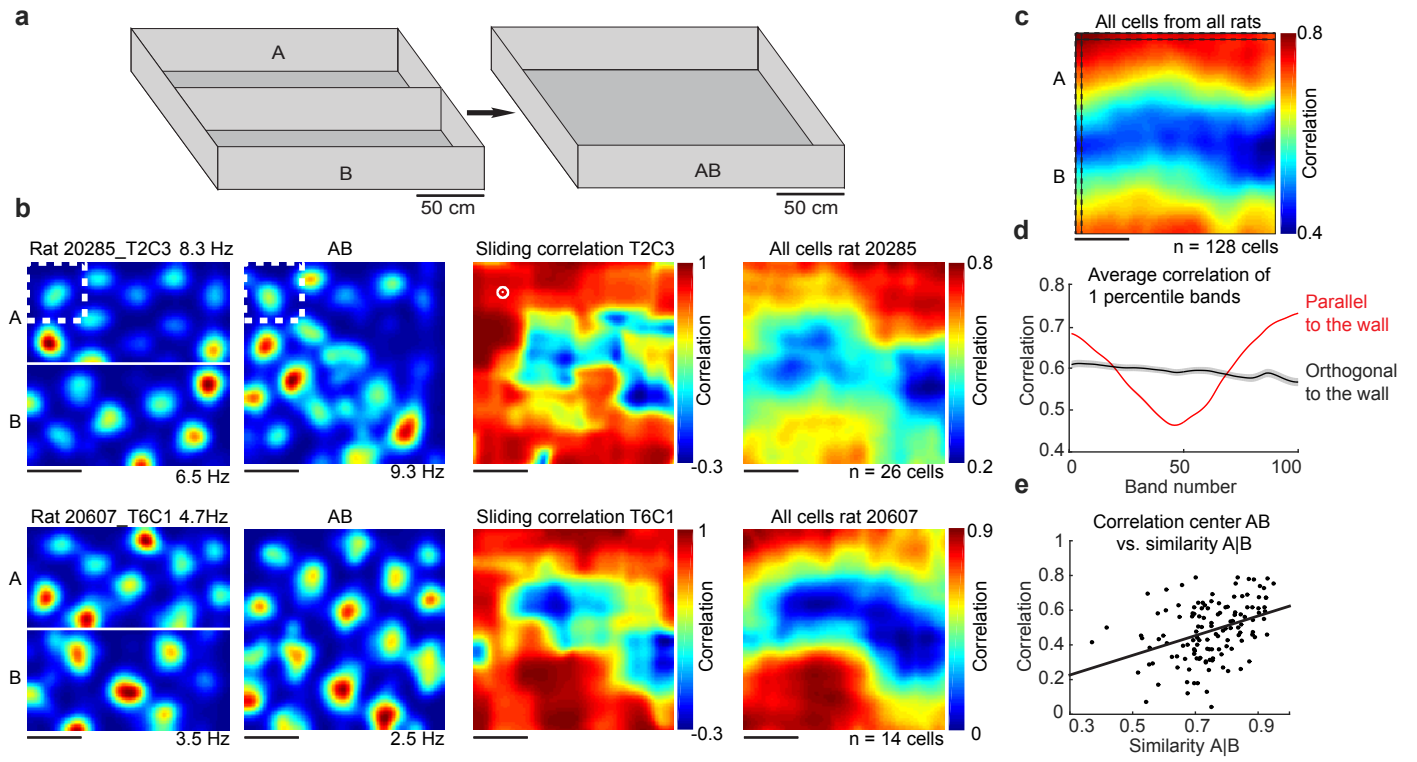


**Figure 2**

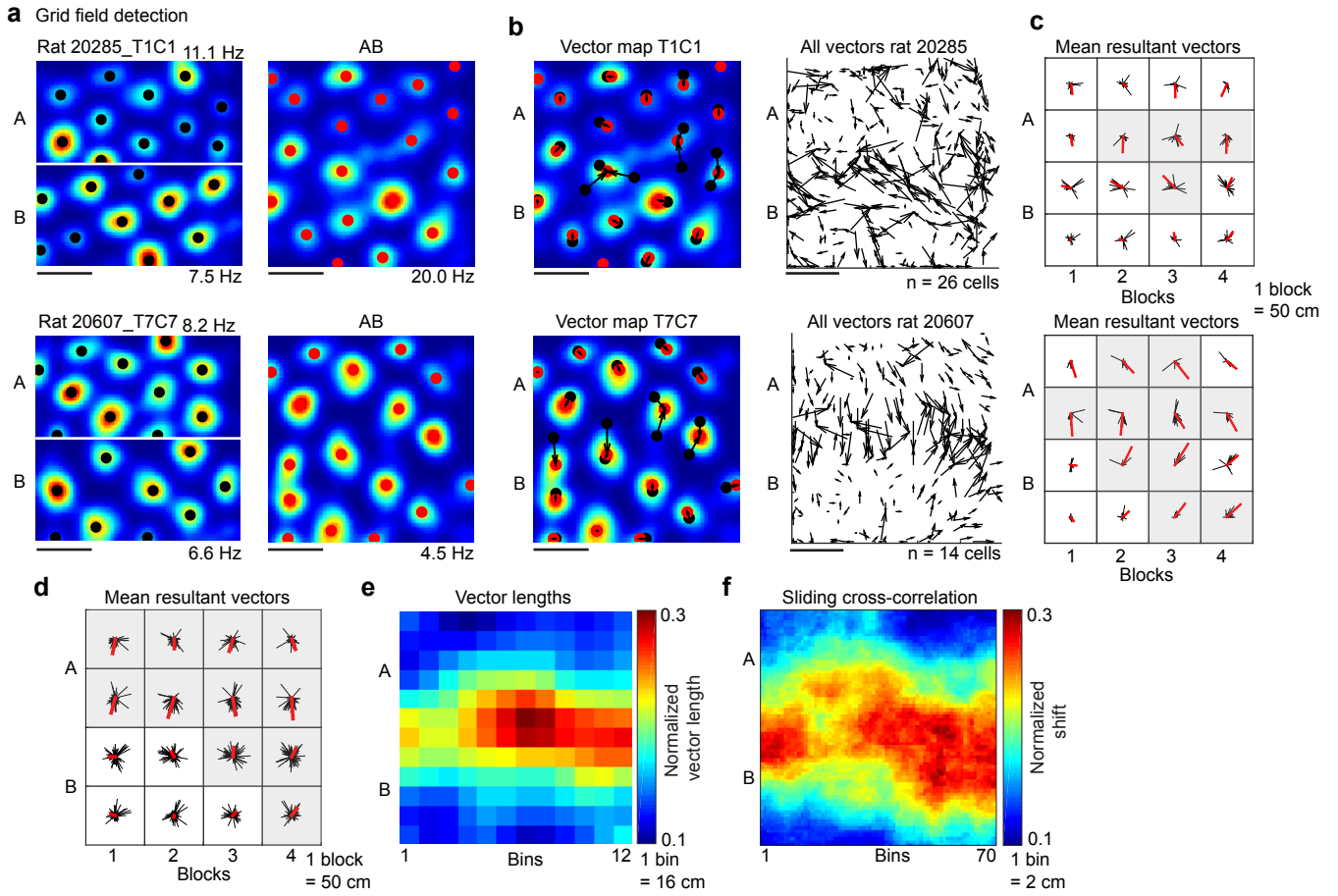


**Figure 3**

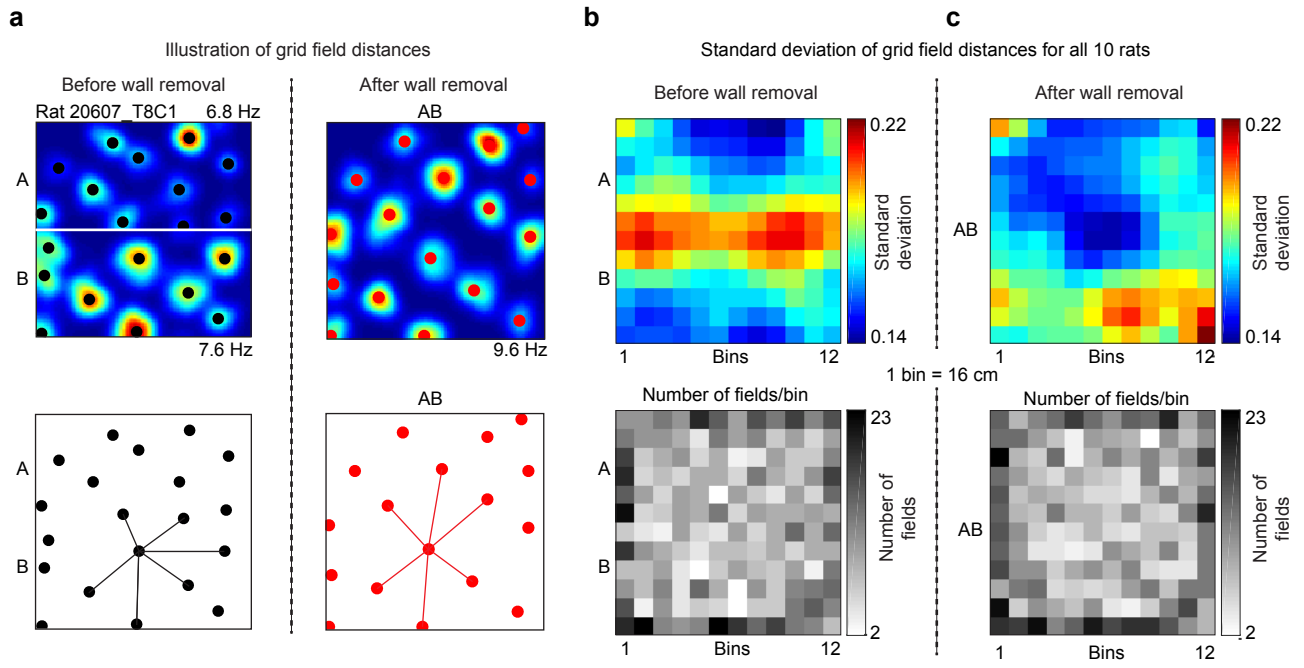


**Figure 4**

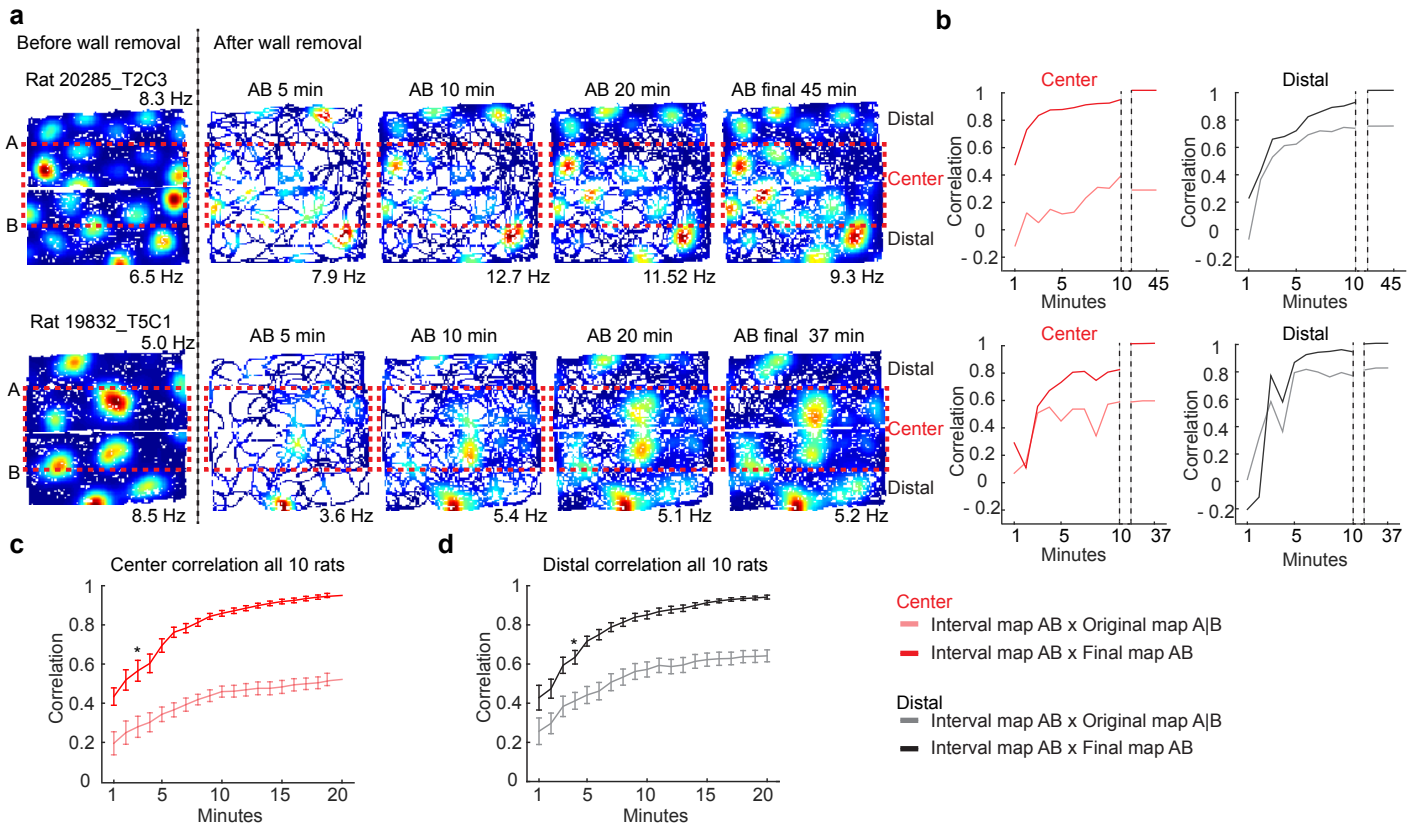


**Figure 5**

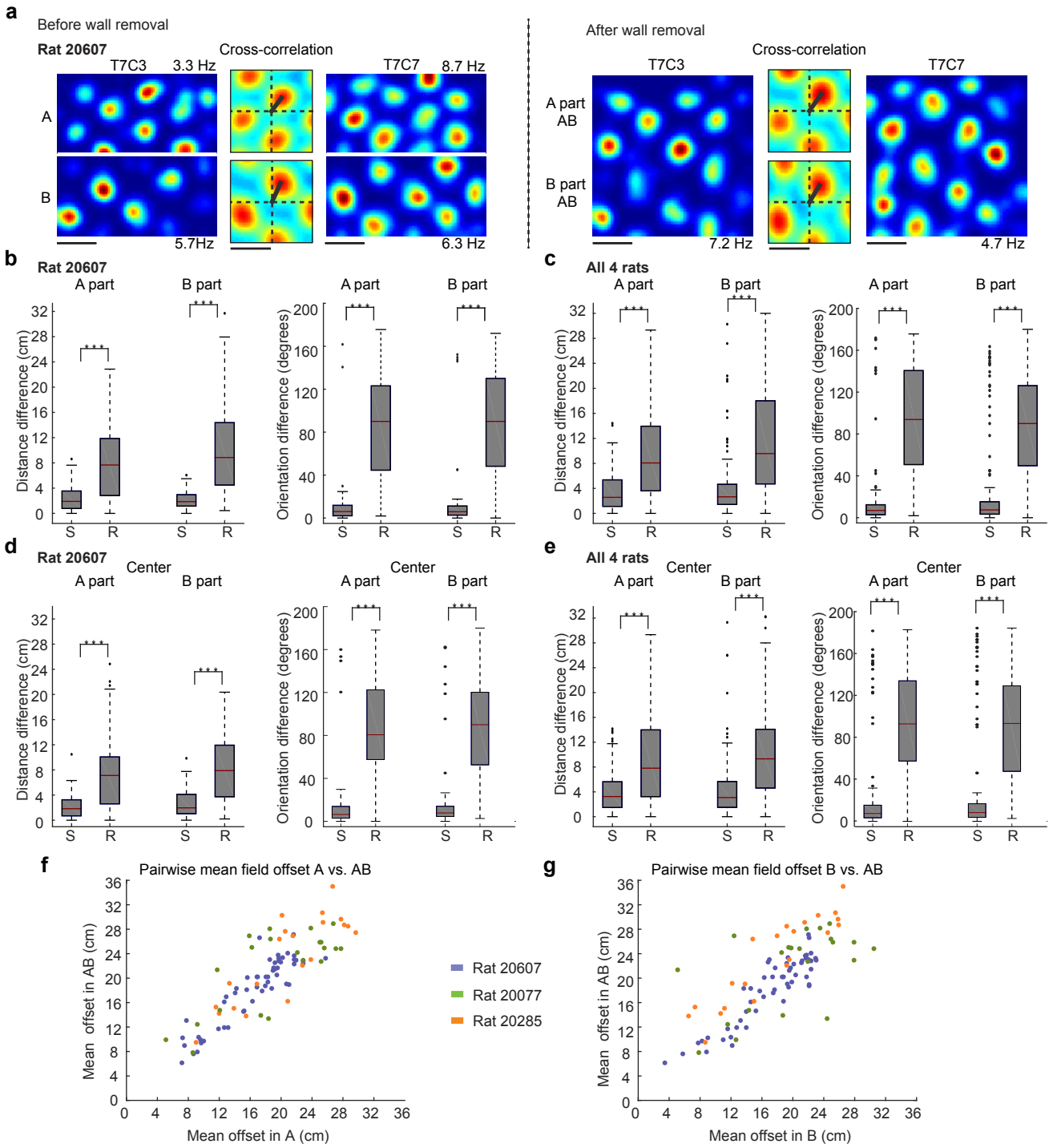
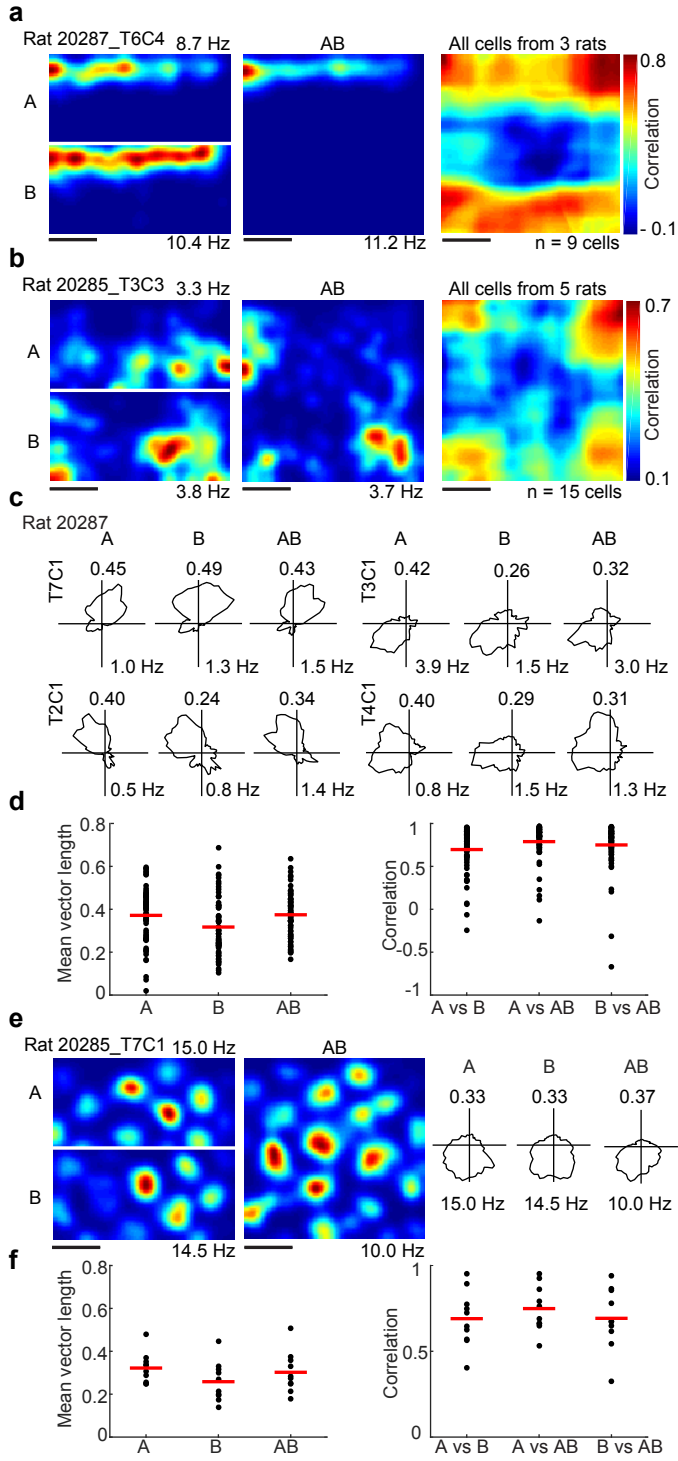
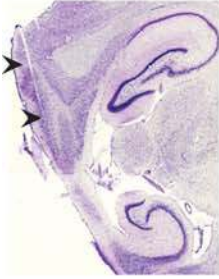




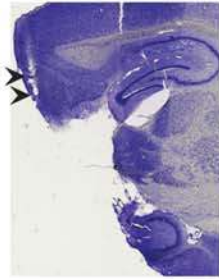
**Figure 6**



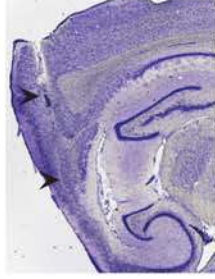
Rat 20077 L\_MEC Layer II



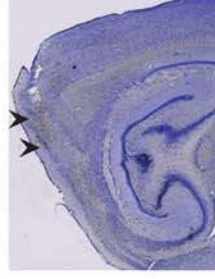
Rat 20607 L\_MEC Layer II



Rat 20288 L\_MEC Layer V to III



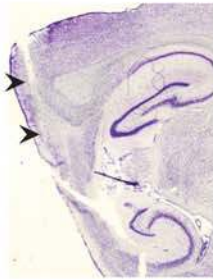
Rat 20288 R\_MEC Layer II



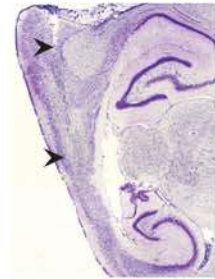
Rat 19871 R\_MEC Layer III to II



Rat 20074 R\_MEC Layer III to II



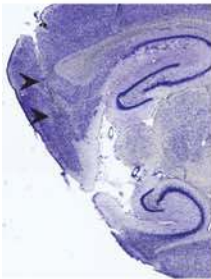
Rat 20075 L\_MEC Layer III to II



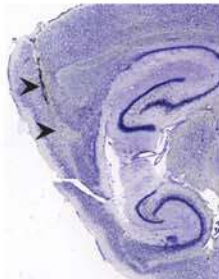
Rat 20284 R\_MEC Layer III to II



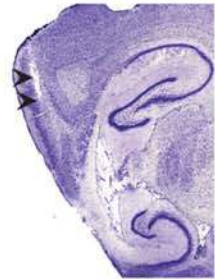
Rat 20285 L\_MEC Layer V to III



Rat 20285 R\_MEC Layer V to III



Rat 20205 L\_MEC Layer III to II



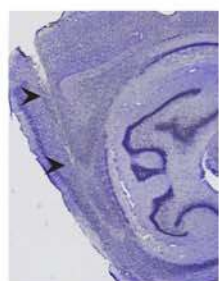
Rat 20205 R\_MEC Layer III to II



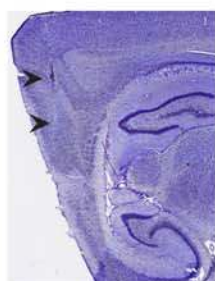
Rat 19832 L MEC Layer III to II



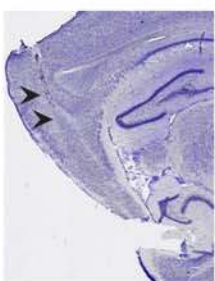
Rat 20204 R MEC Layer V to III



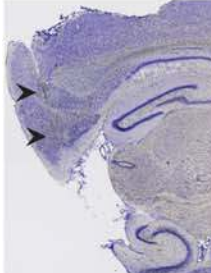
Rat 20206 L MEC Layer V to III



Rat 20206 R MEC/PaS Layer V



Rat 20287 L MEC Layer V



Rat 20287 R MEC/PaS Layer V

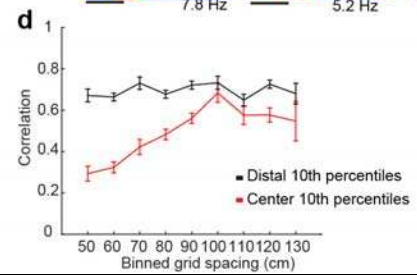
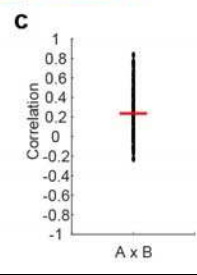
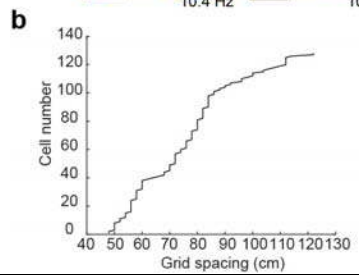
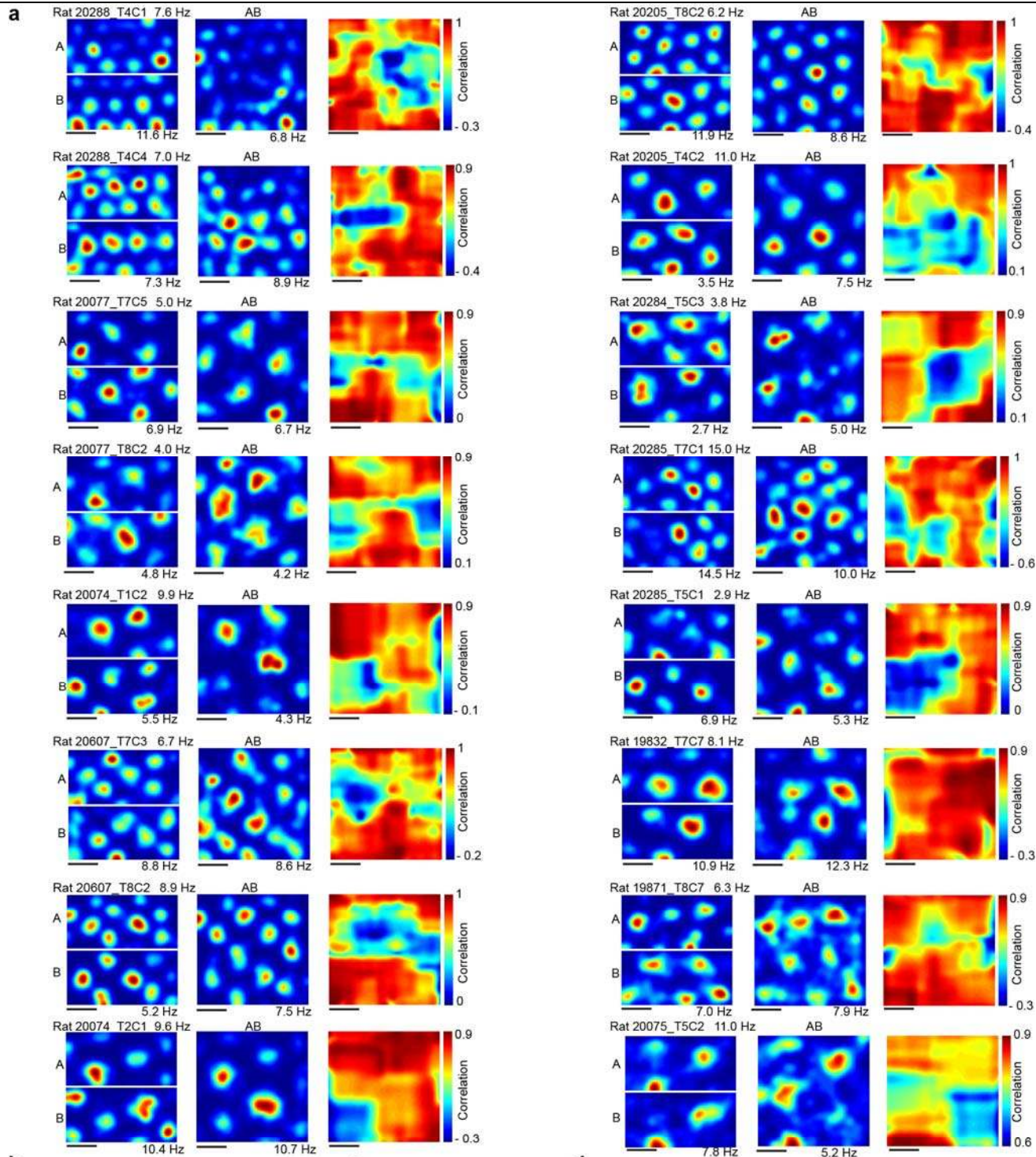


Supplementary Figure 1

**Nissl-stained sagittal sections for 11 rats with grid cells in MEC layers II - V and 2 rats with head direction cells at the MEC-parasubiculum border (PaS).**

Rat identity, brain hemisphere (L = left, R = right), and MEC or MEC-PaS layer are indicated at the top. Black arrowheads indicate the most dorsal and most ventral recording location along the tetrode track.

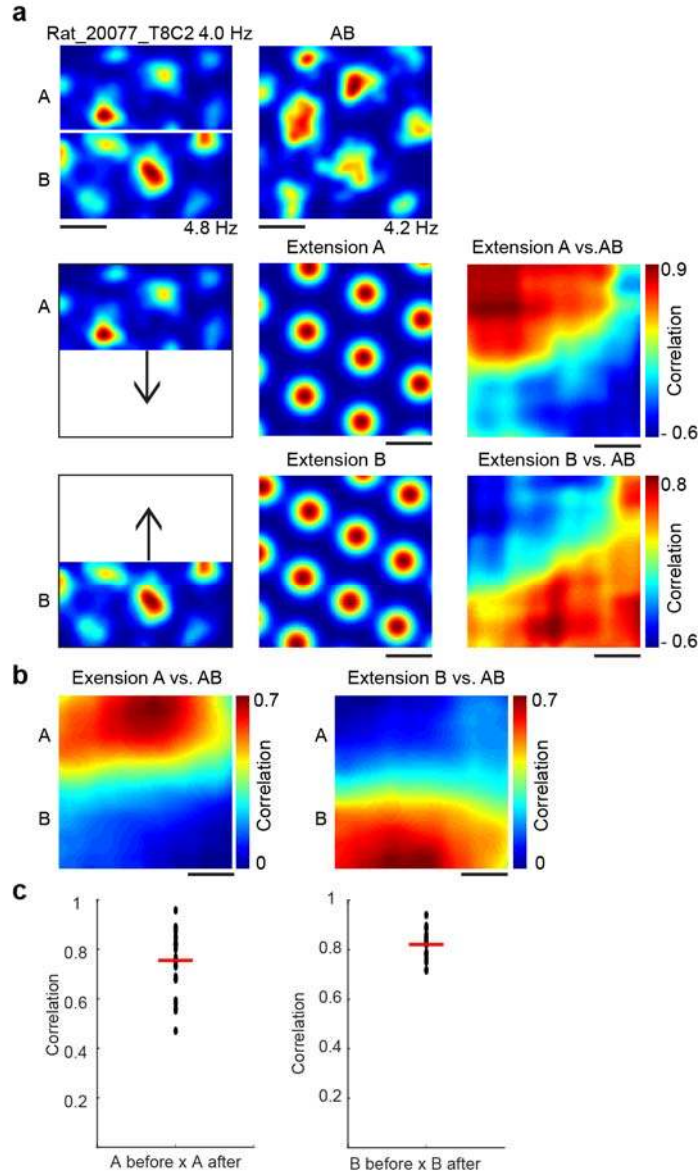




## Supplementary Figure 2

**Representative rate maps in the divided A|B and the merged AB environment and corresponding sliding correlation heat maps A|B x AB for all 10 rats.**

(a) Left: Firing rate maps in A|B and AB. Cell number and rat identity are indicated at the top (t = tetrode, c = cell). Color coded from dark blue (0) to dark red (peak firing rate). Peak Firing rates are indicated at the top and bottom right. Scale bar, 50 cm. Right: Sliding correlation heat map for the cell to the left color-coded from dark blue to dark red (color bar). Scale bar, 50 cm. (b) Distribution of values for mean grid spacing in A, B, and AB across the entire cell population. A wide range of values, with no particular bias, is represented. (c) Ratemaps in A and B were in most cases represented by non-identical grid patterns, although the correlation between rate maps for A and B was higher than expected by chance (Pearson product-moment correlation A vs. B:  $0.237 \pm 0.023$ , one-sample two-sided Student's *t*-test:  $t(127) = 10.4$ ,  $P = 1.14 \times 10^{-18}$ ; correlation A vs. 180-degree rotation of B:  $0.002 \pm 0.021$ ; two-sample two-sided Student's *t*-test for correlation A vs. B against correlation A vs. B rotated:  $t(254) = 7.6$ ,  $P = 7.5 \times 10^{-13}$ ). (d) Line plot showing change in mean correlation between A | B and AB in the central 10% bands and the distal 10% bands as a function of grid spacing. Grid spacing was sorted into bins of 10cm width (mean  $\pm$  s.e.m.,  $n = 128$  cells, 10 rats). Note that, for cells with grid spacing < 90-100 cm, central correlations were lower than distal correlations across the entire range of values for grid spacing, suggesting that reorganization is stronger in the centre than the periphery across several modules. For cells with larger values for grid spacing, correlation values may be inaccurate since larger grids have fewer fields, which mostly touch the distal walls. This, and the frequent absence of fields in the center, may cause inaccuracy in estimates of central field translation.

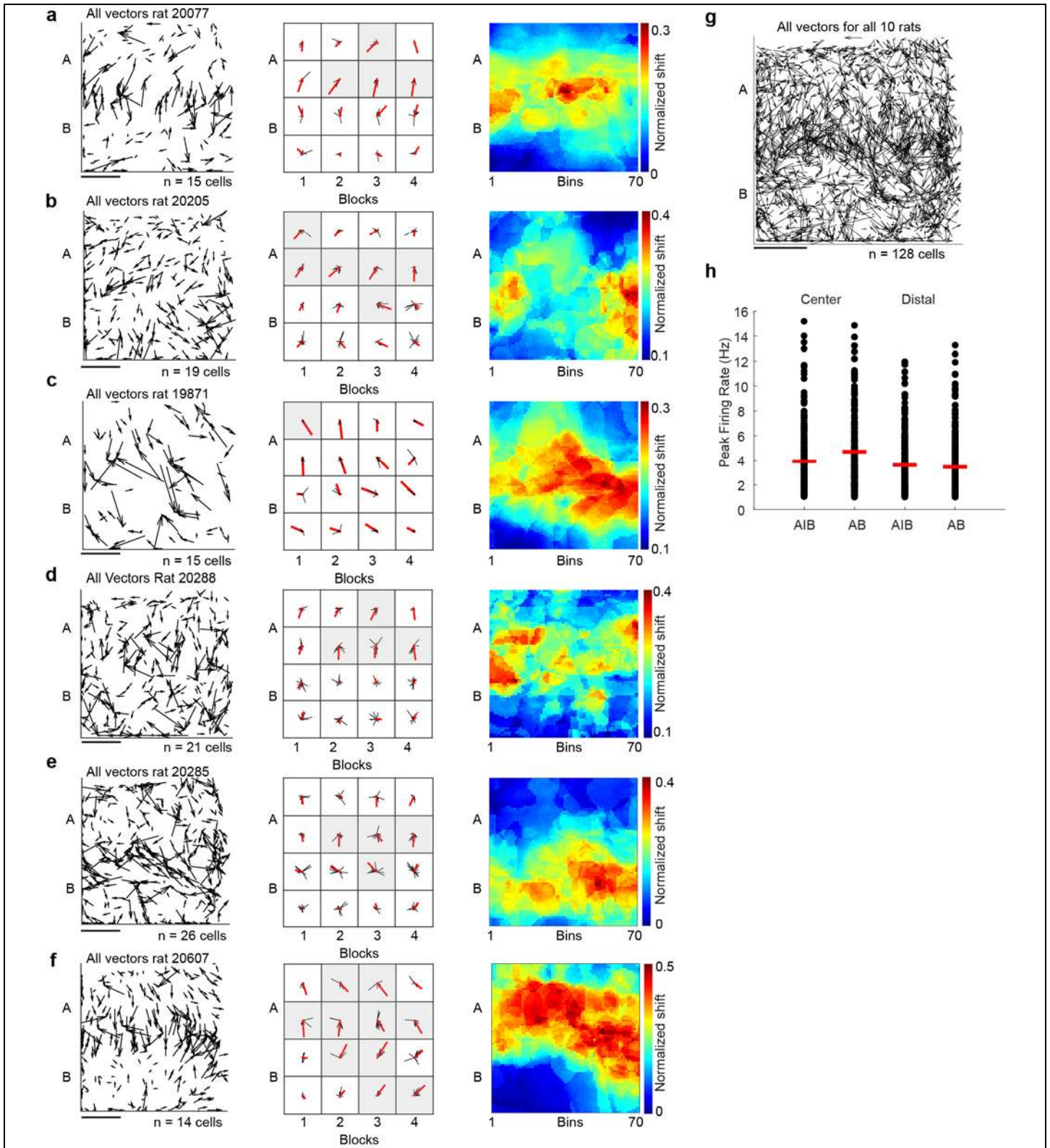


**Supplementary Figure 3**

**The grid pattern in the merged box AB was not a mere extension of the original map in A or B.**

(a) The new map in AB is different from extended A and B maps. Top: Representative firing rate map in the divided A|B environment and the merged environment AB. Scale bar, 50 cm. Center: Simulated grid pattern A extended to the size of the merged map AB (200 x 200 cm) and the corresponding sliding correlation heat map between AB vs. extended pattern A, color-coded from dark blue to dark red (color bar). Scale bar, 50 cm. Bottom: same as center column but for the extended grid pattern of map B. (b) Left: Average sliding correlation heat map extended pattern A x AB for all cells and rats color coded as in a (n = 128 cells, 10 rats). Note that the correlation of the distal 10<sup>th</sup> percentile band of the AB map on the A side was significantly higher with extended map A ( $0.53 \pm 0.02$ ) than with extended map B ( $0.04 \pm 0.02$ , mean  $\pm$  s.e.m., n = 128 cells, 10 rats,  $t(254) = 17.4$ ,  $P = 2.7 \times 10^{-45}$ , two-sided Student's *t*-test). Right: same as to the left but for extended map B. The distal 10<sup>th</sup> percentile band of the AB map had a significantly higher correlation with extended map B ( $0.59 \pm 0.01$ ) than with extended map A ( $0.02 \pm 0.02$ , mean  $\pm$  s.e.m., n = 128 cells, 10 rats,  $t(254) = -16.7$ ,  $P = 5.9 \times 10^{-43}$ , two-sided Student's *t*-test). (c) When the central wall was reintroduced after successive trials in the merged environment, the original grid maps A and B were fully re-expressed. Left: correlation between map A on the last trial before AB and map A on the first trial after AB:  $0.75 \pm 0.02$ , mean  $\pm$  s.e.m., n = 28 cells, 8 rats,  $t(27) = 33.7$ ,  $P = 1.30 \times 10^{-23}$  two-sided Student's *t*-test; Right: same as to the left but for map B:  $0.82 \pm 0.01$ , mean  $\pm$  s.e.m., n = 20 cells, 7 rats,  $t(19) = 60.76$ ,  $P = 13.13 \times 10^{-23}$ , two-sided Student's *t*-test; up to 4 consecutive AB trials intervened between the two trials in the divided environment).



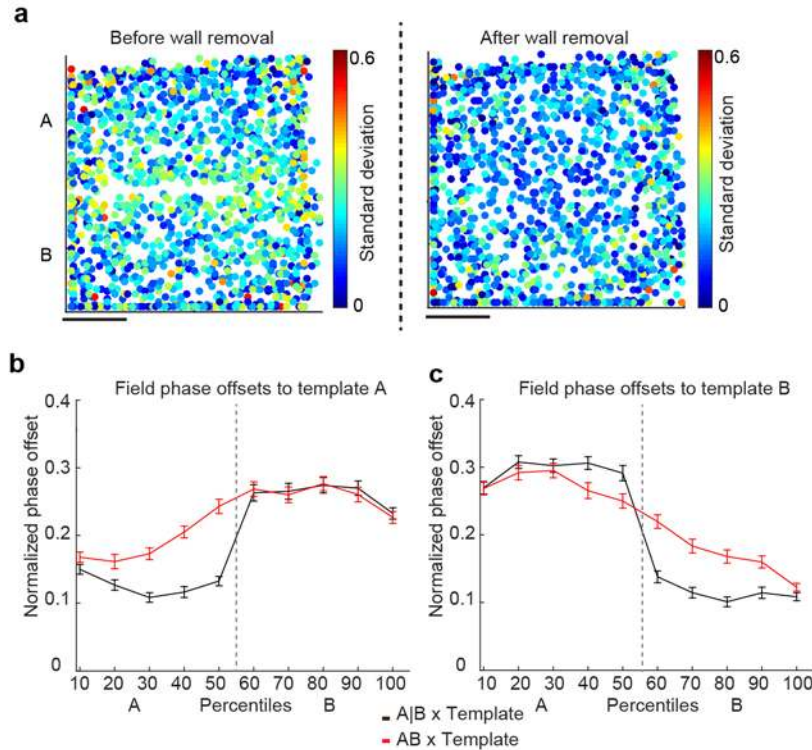


**Supplementary Figure 4**

Translocation of grid fields in the central transition zone of map AB.

**(a)** Left: Vector map for all cells in one rat. Vectors indicate field translocation and point from the original field position in A or B to the nearest field in AB within 60% of the cell's grid spacing in A, B, and AB. Number of cells is indicated at the bottom right. Center: Distribution plots show translation vectors (in black) for blocks of 50 x 50 cm of the recording box. Mean resultant vectors (MVL) are added on top of the single vectors as thick red lines. Grey background shading indicates MVL  $P < 0.001$  with Rayleigh test for uniformity. Right: Average sliding cross-correlation heat map for the cells to the left, color coded from dark blue to dark red (color bar). Shifts were normalized to each cell's average grid spacing in A, B, and AB (1 bin = 2 cm). **(b)- (f)** Further examples from other rats, displayed as in **a**. **(g)** As in **a-f** but the vector map is for all vectors from all cells and rats ( $n = 128$ , 10 rats). To compute average local field displacement, vectors were sorted into square windows of side length 16 cm and averaged (see **Fig. 2c**). **(h)** The displacement of firing fields in the centre of the box was accompanied by a change in peak firing rates of grid fields that could be matched before and after removal of the wall. After the wall was removed, the peak firing rate of grid fields in the central 10<sup>th</sup> percentile bands increased from  $3.91 \pm 0.15$  Hz in A | B to  $4.70 \pm 0.18$  Hz in AB ( $t(548) = -3.32$ ,  $P = 9.5 \times 10^{-4}$ , two-sided Student's t-test; peak rate defined as the rate in the central bin of the grid field). In the distal 10<sup>th</sup> percentile bands, there was no significant change in firing rates (before:  $3.61 \pm 0.12$  Hz; after:  $3.44 \pm 0.12$  Hz;  $t(692) = 0.92$ ,  $P = 0.35$ , two-sided Student's t-test).

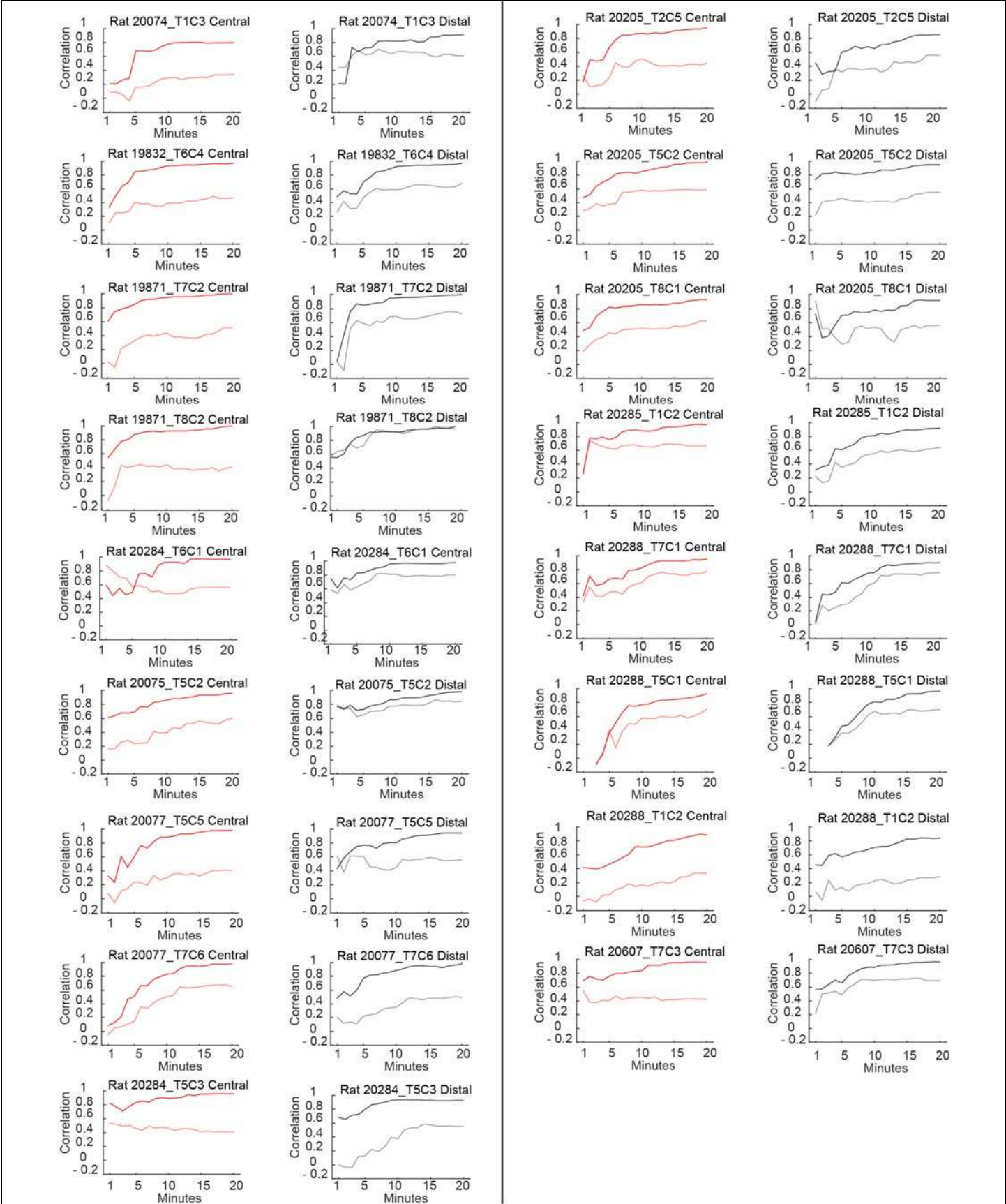




## Supplementary Figure 5

### Establishment of a locally continuous grid pattern in the merged environment.

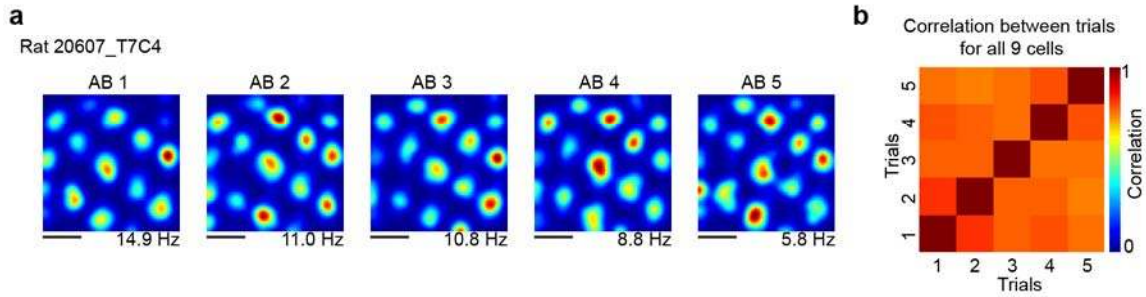
(a) Standard deviation of grid field distances for all grid fields from all rats. Left: Before wall removal. Each dot represents one grid field and is color coded according to the standard deviation of distances to all neighboring fields within 130% of the cell's average grid spacing in A, B, and AB (blue = minimum standard deviation in A|B and AB; red = maximum standard deviation in A|B and AB;  $n=128$  cells, 1576 fields, 10 rats). Right: After wall removal ( $n=128$  cells, 1447 fields, 10 rats). To compute average local standard deviations, standard deviations were sorted into square windows of side length 16 cm and averaged (see Fig. 3b, c). Scale bar, 50cm. (b) Local grid field offset as a function of distance from partition wall. Average field offset between A|B or AB and a template grid pattern determined from A (A|B vs. template in black; AB vs. template in red; offsets are binned into 10<sup>th</sup> percentile bands of 200 x 20 cm each, mean  $\pm$  s.e.m.,  $n=128$  cells). Grey stippled line indicates location of the former partition wall. (c) As in a but for a template pattern determined from B. Note, before wall removal phase offsets change abruptly in the center percentiles and approximate a step function. After wall removal, phase offsets change more linearly between A and B, indicating translocation of single grid fields into a pattern that is locally continuous throughout the environment. To quantify this transition, a linear regression was fit to the data from 10% bands spanning from the distal north wall in A to the distal south wall in B, as well as a step function with the step at the position of the partition wall. The residual mean square root (r.m.s.) for differences between data and step function increased when the wall was removed (r.m.s. expressed as percentage grid spacing for A|B vs. AB: 2.0% vs. 4.0%, square residuals A|B vs. AB:  $t(38) = 2.1$ ,  $P = 0.04$ , two-sided Student's *t*-test). The residual mean square root for differences between data and linear regression decreased (r.m.s. A|B vs. AB: 4.3% vs. 2.2%, square residuals A|B vs. AB:  $t(38) = 3.9$ ,  $P = 3.3 \times 10^{-4}$ , two-sided Student's *t*-test), suggesting that translocation of firing locations decreased gradually with distance from the partition wall. This trend was generally upheld when we analyzed data from subsets of grid cells with either small or large grid scales (small: 44 cm to 61 cm,  $n=38$  cells, r.m.s. step function A|B vs. AB: 2.4% vs. 3.6%, r.m.s. linear regression A|B vs. AB: 3.6% vs. 2.0%; large-scale grid cells range: 84 cm to 136 cm,  $n=38$  cells, r.m.s. step function A|B vs. AB: 2.9% vs. 4.9%, r.m.s. linear regression A|B vs. AB: 3.5% vs. 2.1%). The progression towards a linear change in offsets from the template indicates that local grid coherence increased throughout the environment.



## Supplementary Figure 6

### Development of firing rate distribution during the first trial in the merged environment AB for all cells and rats.

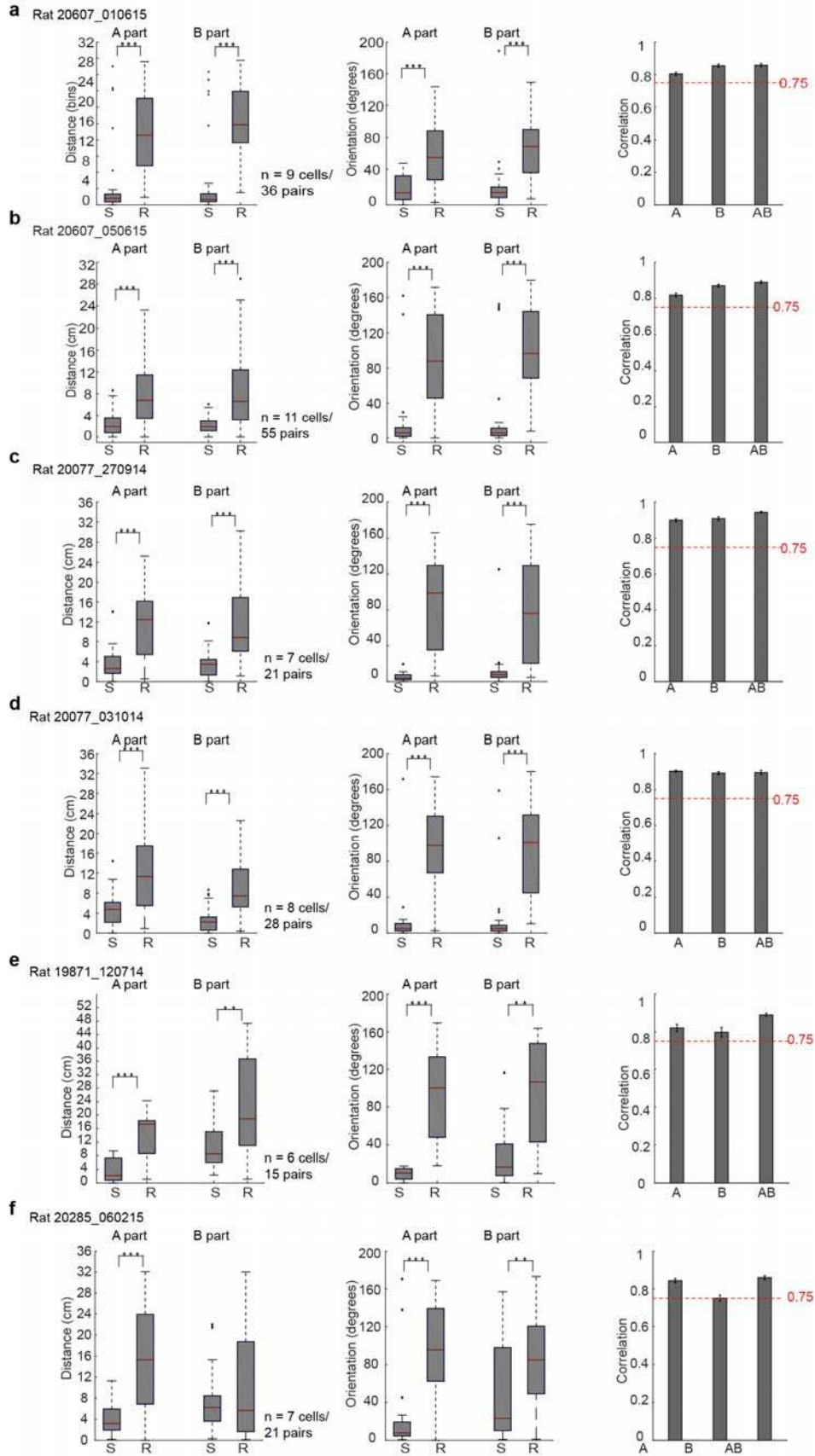
Left column of each panel: correlation of interval rate maps for cumulative 1-min blocks in AB vs. the corresponding rate map for the entire trial in either A|B (light red line) or AB (dark red line). Only the central half of the environment is included in the correlation analysis (center half of A, center half of B; together they covered 200 cm x 100 cm of the box). Time intervals increased cumulatively by 60s (block 1 is for 0-1 min, block 2 for 0-2 min, block 3 for 0-3 min, etc). Rat number and cell identity are indicated at the top (T = tetrode, C = cell). Right column: same as to the left but for the distal half of A|B (light grey line) or AB (dark grey line). Also here the distal half of A and distal half of B covered together 200 cm x 100 cm.



### Supplementary Figure 7

#### Grid cell patterns are stable across consecutive trials in AB.

(a) Example rate maps for one grid cell recorded across 5 consecutive trials in AB after the wall was removed for the third time (trial numbers are indicated on the top, trial numbers AB1 to AB5 correspond to the 8<sup>th</sup> to the 12<sup>th</sup> exposure in the merged box). Peak firing rates are indicated at the bottom right. Rat identity and cell number is indicated at the top (T = tetrode, C = cell). Scale bar, 50cm. (b) Average correlation between pairs of 5 consecutive trials in AB for 9 simultaneously recorded grid cells including the cell in a, color-coded from dark blue to dark red (color bar). Grid cells shared the same spacing and orientation. Note, all pairwise correlation values between trials were high, suggesting that in each cell, grid field locations showed little change between consecutive trials in AB.

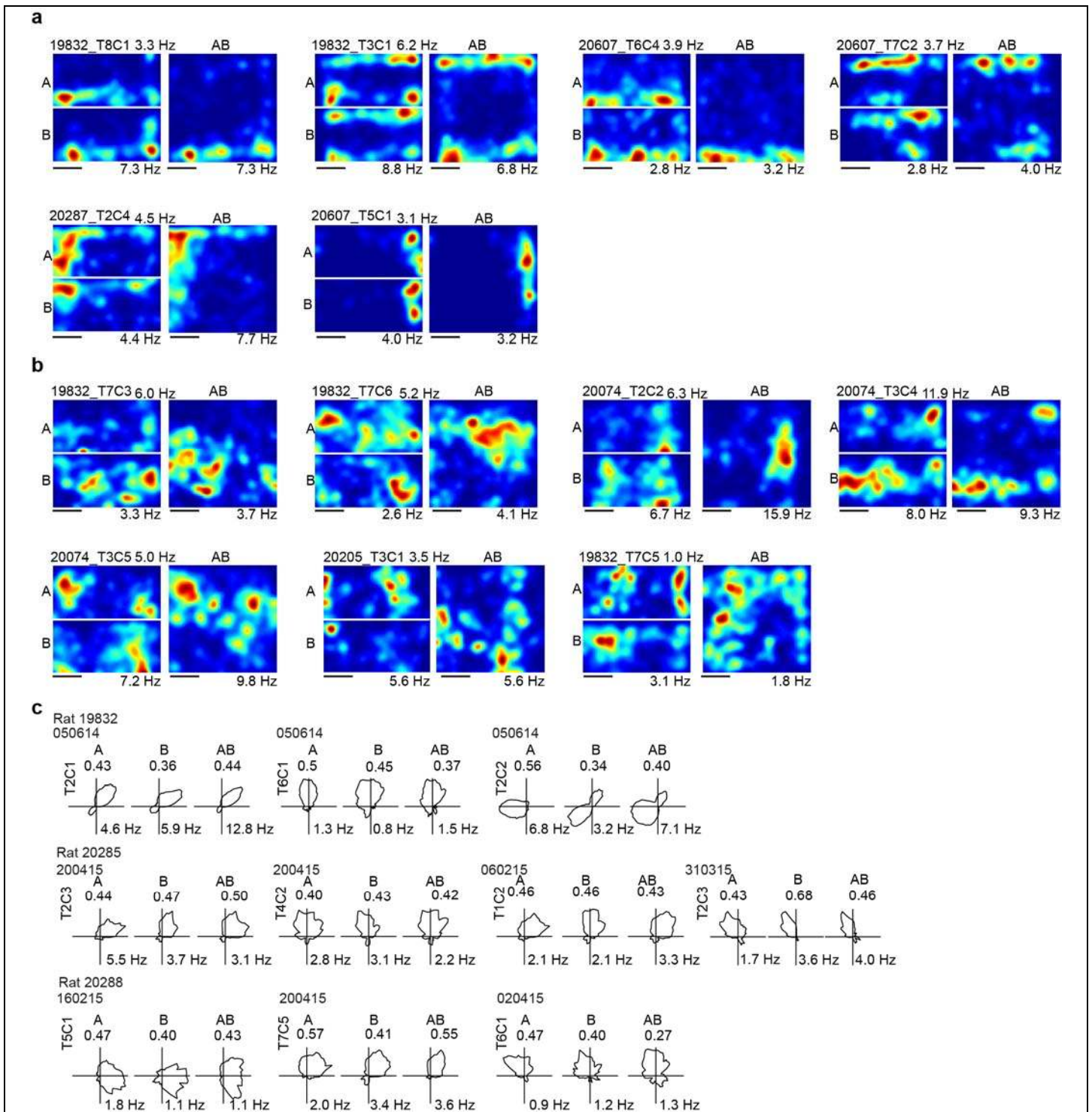


## Supplementary Figure 8

### Phase relationships between pairs of grid cells were maintained after removal of the central partition wall.

(a) Left: Average difference in distance offset between same (S) and randomly (R) chosen cell pairs. Data are plotted as in **Fig. 5b,c**. Red line indicates median difference in offset of the displaced center peak, box edges indicate 25<sup>th</sup> and 75<sup>th</sup> percentiles, whiskers extend to the last data point that lies within 1.5 times the interquartile range, and data points larger than 1.5 times the interquartile range are considered outliers (black dots). Rat number and trial date are indicated at the top. Number of cells and cell pairs are indicated at the bottom right ( $***P < 0.001$ , two-sided Wilcoxon rank sum test). Center: Average angular difference of orientation offset between same and random cell pairs ( $***P < 0.001$ , Watson  $U^2$  test). Right: Pairs of grid cells share the same orientation and spacing. Average correlation of autocorrelograms for all cell pairs. Stippled red line indicates 90<sup>th</sup> percentile of all pairwise correlations from all cells and rats ( $n = 128$  cells / 8128 pairs). (b) – (f) As in **a** but for different trials or animals ( $**P < 0.05$ , Watson  $U^2$  test).





**Supplementary Figure 9**

**Representative border cells, non-periodic spatially modulated cells, and head direction cells.**

(a) Representative firing rate maps for 6 border cells from 3 rats for the divided A|B environment and the merged AB environment. Peak firing rates are indicated at the bottom right. Rat identity and cell number is indicated at the top (T = tetrode, C = cell). Scale bar, 50 cm. (b) As in a but for 7 non-periodic spatially modulated cells from 3 rats in A|B and AB. Scale bar, 50 cm. These cells had high spatial information content and stable firing locations (spatial information value of  $0.82 \pm 0.05$  and spatial correlation between first and second

half of trial of  $0.49 \pm 0.03$ ; all trials and all parts of environment, mean  $\pm$  s.e.m). (c) Polar plots of angular firing rate distribution for 10 representative head direction cells from 3 rats in A, B, and AB. Rat number and trial date are indicated at the top. Cell number is indicated at the left site (T = tetrode, C = cell). Mean resultant vector length, a measure for directional tuning, is indicated at the top in each plot. Peak firing rate is indicated at the bottom right.